The Astrophysical Journal, 832:174 (19pp), 2016 December 1 doi:10.3847/0004-637X/832/2/174

A VERY BRIGHT, VERY HOT, AND VERY LONG FLARING EVENT FROM THE M DWARF BINARY SYSTEM DG CVn

Rachel A. Osten[1,16], Adam Kowalski[2,3,4], Stephen A. Drake[5], Hans Krimm[6], Kim Page[7], Kosmas Gazeas[8], Jamie Kennea[9], Samantha Oates[10], Mathew Page[11], Enrique de Miguel[12,17], Rudolf Novák[13], Tomas Apeltauer[14], and Neil Gehrels[15]
[1] Space Telescope Science Institute, USA osten@stsci.edu
[2] U. Md/GSFC, USA
[3] Department of Astrophysical and Planetary Sciences, University of Colorado, Boulder, 2000 Colorado Ave., Boulder, CO 80305, USA
[4] National Solar Observatory, University of Colorado, Boulder, 3665 Discovery Drive, Boulder, CO 80303, USA
[5] USRA/CRESST and NASA/GSFC, USA
[6] USRA/CRESST, USA
[7] X-ray and Observational Astronomy Group, Department of Physics & Astronomy, University of Leicester, Leicester, LE1 7RH, UK
[8] Department of Astrophysics, Astronomy and Mechanics, University of Athens, GR-15784 Zografos, Athens, Greece
[9] Penn State, USA
[10] Instituto de Astrofsica de Andalucía (IAA-CSIC), Glorieta de la Astronomía s/n, E-18008, Granada, Spain
[11] Mullard Space Science Laboratory, University College London, Holmbury St. Mary, Dorking RH5 6NT, UK
[12] Departamento de Fisica Aplicada, Facultad de Ciencias Experimentales, Universidad de Huelva, E-21071 Huelva, Spain
[13] Research Centre for Toxic Compounds in the Environment, Faculty of Science, Masaryk University, Kamenice 3, 625 00 Brno, Czech Republic
[14] Brno University of Technology, Faculty of Civil Engineering, Veveri 331/95, 602 00 Brno, Czech Republic
[15] NASA/GSFC, USA
Received 2016 July 29; revised 2016 September 14; accepted 2016 September 15; published 2016 November 30

ABSTRACT

On 2014 April 23, the *Swift* satellite responded to a hard X-ray transient detected by its Burst Alert Telescope, which turned out to be a stellar flare from a nearby, young M dwarf binary DG CVn. We utilize observations at X-ray, UV, optical, and radio wavelengths to infer the properties of two large flares. The X-ray spectrum of the primary outburst can be described over the 0.3–100 keV bandpass by either a single very high-temperature plasma or a nonthermal thick-target bremsstrahlung model, and we rule out the nonthermal model based on energetic grounds. The temperatures were the highest seen spectroscopically in a stellar flare, at T_X of 290 MK. The first event was followed by a comparably energetic event almost a day later. We constrain the photospheric area involved in each of the two flares to be $>10^{20}$ cm^2, and find evidence from flux ratios in the second event of contributions to the white light flare emission in addition to the usual hot, $T \sim 10^4$ K blackbody emission seen in the impulsive phase of flares. The radiated energy in X-rays and white light reveal these events to be the two most energetic X-ray flares observed from an M dwarf, with X-ray radiated energies in the 0.3–10 keV bandpass of 4×10^{35} and 9×10^{35} erg, and optical flare energies at E_V of 2.8×10^{34} and 5.2×10^{34} erg, respectively. The results presented here should be integrated into updated modeling of the astrophysical impact of large stellar flares on close-in exoplanetary atmospheres.

Key words: stars: coronae – stars: flare – stars: individual (DG CVn)

1. INTRODUCTION

Most of what is known about the mechanisms producing stellar flares is informed by the detailed observations of flares on the Sun. Solar flares occur in close proximity to active regions (ARs), which are effectively localized magnetic field regions of 1–2 kG strength. Loops from these ARs extend into the solar corona; as the footpoints of these loops are jostled by solar convective motions, they are twisted and distorted until magnetic reconnection occurs near the loop tops (Parker 1988; Benz & Güdel 2010). The reconnection event is accompanied by a sudden release of energy, resulting in the acceleration of electrons and ions in these loops up to MeV energies, which stream both toward and away from the Sun, emitting nonthermal radio (gyrosynchrotron) and X-ray emission (particularly at the loop footpoints) as they move (Dennis & Schwartz 1989). These energetic particles stream down to the loop footpoints and deposit substantial energy to the lower solar atmosphere (the chromosphere), "evaporating" and heating plasma from this region to fill the flaring loop(s) with plasma (Lin 2011). In the "decay" phase of the flare, the thermal emission dominates the X-ray emission, though in some large solar flares a nonthermal X-ray component may persist as a continuous source of energy (Kontar et al. 2008).

Young stars and stars in close binary systems rotate much more rapidly than the Sun, and, in consequence, have much stronger levels of magnetic activity, i.e., greater coverage by starspots and ARs, stronger chromospheric and coronal emission, and more frequent and powerful flares (Meibom et al. 2007; Morgan et al. 2016). There is a large disparity between the extremes of solar and stellar flares: while the largest solar flares have radiated energies exceeding 10^{32} erg, and maximum coronal temperatures of a few tens of MK (Sharykin et al. 2015), large stellar flares can be 10^6 times more energetic, with coronal temperatures around 100 MK (Osten et al. 2007) and large energetic releases up to 10^{38} erg (Kuerster & Schmitt 1996; Osten et al. 2007). A 2008 flare of the nearby 30–300 Myr old M dwarf flare star EV Lac (Osten et al. 2010) had a lower limit on the energetic release of 6×10^{34} erg. Caramazza et al. (2007) found X-ray flares on very young low-

[16] Also at Center for Astrophysical Sciences, Johns Hopkins University, Baltimore, MD 21218.
[17] Also CBA-Huelva, Observatorio del CIECEM, Parque Dunar Matalascañas, 21760 Almonte, Huelva, Spain.

mass stars to range up to 2×10^{35} erg, and Tsuboi et al. (2014) found flares from active binary systems to range up to 10^{38} erg. The interpretation of these stellar flaring events assumes that the same physical processes are at work as in the solar case, as confirmed by multi-wavelength observations of plasma heating and particle acceleration in stellar flares (Benz & Güdel 2010). The largest stellar flares, with their extreme parameters of temperature and energy release, clearly test this correspondence. Initial suppositions of a transition from solar-stellar flare scaling laws has come from the work of Getman et al. (2008), but those data could not determine flare temperatures accurately.

DG CVn (GJ 3789) is an interesting, albeit poorly studied member of this class of nearby, very young low-mass stars. It is noted as having an unusually active chromosphere (Beers et al. 1994) and corona (Hünsch et al. 1999), as well as being one of the brightest nearby stellar radio emitters (Helfand et al. 1999). Subsequent studies confirm that it exhibits optical flares and sub-day rotational modulation (Robb 1994), with a measured photospheric line broadening of 51 km s^{-1} (Mohanty & Basri 2003) indicative of a very short rotational period of <8 hr. DG CVn is a binary, as revealed by the double-lined spectrum noted in Gizis et al. (2002). Adaptive optics imaging of DG CVn (Beuzit et al. 2004) reveal it to be a close (0.″2 separation) visual binary system, with two components of near-equal optical brightness ($\Delta V \sim 0.3$) and spectral types of M4Ve. The distance to DG CVn, from a large study of the trigonometric parallaxes and kinematics of nearby active stars, is 18 pc, with a space motion consistent with the system being a member of the population of 30 Myr old stars in the solar neighborhood (Riedel et al. 2014). They quote a combined systemic $\log L_X$ and $\log L_X/L_{\rm bol}$, from which (by dividing $L_{\rm bol}$ equally between the two components) a luminosity of $\log(L_{\rm bol}/L_\odot) = -1.72$ is obtained. Mohanty & Basri (2003) determine a system $T_{\rm eff}$ of 3175 K, which combined with $L_{\rm bol}$ yields a radius estimate of 0.46 $R_\odot$. Demory et al. (2009) plot stellar radius versus absolute magnitude in the K band, $M(K)$, for low-mass and very-low-mass stars using interferometric measurements; their 5 GY isochrones together with the absolute K magnitude of the A component of the binary (6.12; Riedel et al. 2014) suggests a radius of about 0.4 $R_\odot$. These numbers are consistent with a larger radius than obtained for other nearby M dwarfs of the same temperature (such as described in Mann et al. 2015; Newton et al. 2015) and we adopt $R_\star = 0.4 R_\odot$ in this paper. In young stars, accretion episodes can provide an additional optical and X-ray signature to that expected from magnetic reconnection (Stassun et al. 2006; Brickhouse et al. 2010). However, the *WISE* $w_1 - w_3$ and $w_1 - w_4$ colors of this system show no evidence for an infrared excess (Cutri et al. 2013), indicating that there is no active accretion, as would be expected for stars older than several million years.

On 2014 April 23, one of the two stars in this system flared to a level bright enough ($\sim 3.4 \times 10^{-9}$ erg s^{-1} cm^{-2}) in the 15–100 keV band that it triggered the *Swift* Burst Alert Telescope (BAT); described in Drake et al. (2014). Two minutes later, after *Swift* had slewed to point in the direction of this source, the *Swift* X-ray Telescope (XRT) and the Ultraviolet Optical Telescope (UVOT) commenced observing this flare. These observations, as well as supporting ground-based optical and radio observations, continued (intermittently) for about 20 days and yielded a fascinating case history of this colossal event, the decay of which took more than two weeks in the soft X-ray band, and included a number of smaller superimposed secondary flares (see Figure 1). Recent papers have reported on additional data indicating radio and optical bursts from this system during this time period (Caballero-García et al. 2015; Fender et al. 2015). In this paper, we discuss the observations and their interpretation in light of the standard solar flare scenario. The paper is organized as follows. Section 2 describes the entire set of *Swift* and ground-based observations used in the study, Section 3 describes the analysis of the two main flaring events observed, Section 4 discusses what can be determined for the second event, and applies this to an interpretation of the first event, and, finally, Section 5 provides our conclusion.

2. OBSERVATIONS

2.1. Swift/BAT Data

The *Swift*-BAT instrument (Barthelmy et al. 2005) triggered on the flare from DG CVn at 2014 April 23 UT 21:07:08.0 = T0 (BAT trigger number 596958). The source location was in the BAT field of view (FOV) starting from T–1627 s, but there was no detectable emission until approximately T−40 s. After the trigger occurred, a slew placed the star in the apertures of the narrow-field instruments (XRT and UVOT), for 210 s on target before an observing constraint led to a slew to another target. However, DG CVn remained in the BAT FOV during this new pointing, until T+892 s. The mask-weighted light curve shows a single peak from ∼T0–40 s to 120 s and another weaker peak from ∼T0+200 to T0+240 s. BAT spectra from 15 to 150 keV were extracted for the time intervals from T0−30 s to T0+72 s and from T0+123 to T0 +328 s (the latter to match the initial XRT observation), and are shown in Figure 2.

2.2. Swift/XRT Data

The XRT (Burrows et al. 2005) began observing DG CVn 117 s after the BAT trigger. The online XRT product generator[18] (Evans et al. 2007, 2009) was utilized to produce the XRT light curve and extract the time-sliced spectra. This tool was used to account for pile-up and to apply all necessary corrections. At the time of writing, the software version used by the generator was HEASoft 6.18, with the calibration file release of 2016 January 21.

For the initial snapshot of data, immediately following the BAT trigger, the data were collected in Windowed Timing (WT) mode, due to the large count rate. Observations between 4.5 and 50 ks after the trigger occurred using a combination of both WT and Photon Counting (PC) modes; all later data were then taken in PC mode.

2.3. Swift/UVOT Data

The UVOT (Roming et al. 2005) began observing DG CVn, 108 s after the *Swift*-BAT trigger, T0, with a 10 s settling exposure. After a 4.2 ks gap in XRT/UVOT observations, UVOT observed in all seven UVOT filters with regular cadence until 1.7 Ms after the trigger. The UVOT returned to the field four months later (11 Ms after the trigger) to determine the quiesent level in the optical and UV filters. Upon

[18] http://www.swift.ac.uk/user_objects/

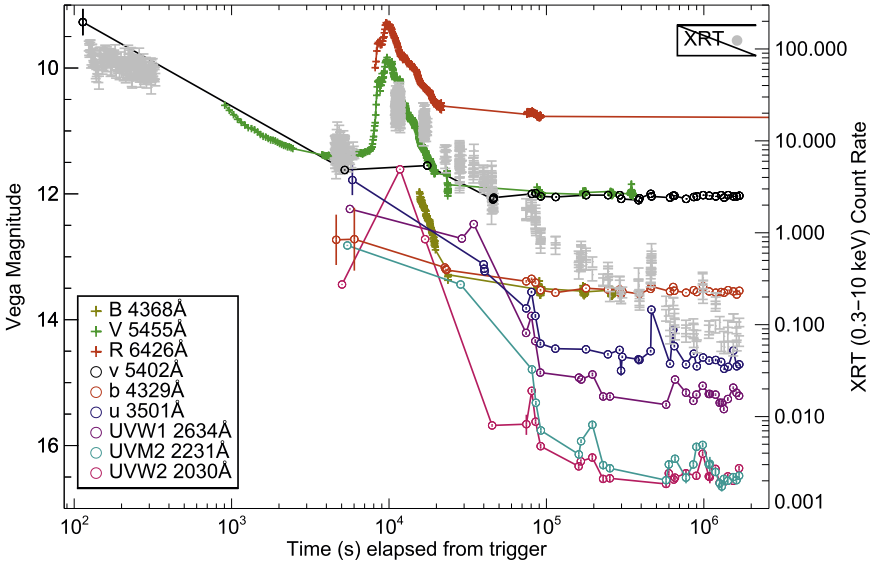

Figure 1. Comprehensive light curve of the event as seen in soft X-rays, UVOT bands, and ground-based optical photometry. The initial impulsive event took only a few hours to decay, but was followed by a series of flares that spanned more than two weeks. The legend lists the UV optical filters and the central wavelength of each.

examination of the initial images, we found that all the white exposures were saturated and therefore no futher exposures were taken later than 11.5 ks. The *v* settling image and the first two *b* and *u* exposures were also saturated. Observations continued from 74 ks for the *v*, *b*, and *u* filters in hardware mode since the quiescent *V* band magnitude for DG CVn is close to the brightness limit of the standard UVOT image mode. In this case, a smaller portion of the detector was read out, reducing the frame time of each exposure from 11 to 3 ms and enabling brighter objects to be observed.

To perform the photometry for non-saturated images, we used a region of 5″ radius to extract the source counts and background counts were extracted using two circular regions of radius 12″ from a blank area of sky situated near to the source position. The count rates were obtained from the images using the *Swift* tools uvotsource. For the saturated images, we were able to extract photometry from the first *v* exposure, the first two *b* exposures and the second *u* band exposure using the read out streaks associated with DG CVn, taking advantage of the method recently developed by Page et al. (2013). The resulting error bars for these exposures reflect the larger photometric uncertainty using this method. We note that the first *v* exposure is trailed; however, because this exposure was observed in event mode, we were able to extract a new image excluding the affected, first 2.2 s. The resulting count rates from both photometric methods were converted to magnitudes using the UVOT photometric zero points (Breeveld et al. 2011).

2.4. University of Athens Observatory R-band Data

Relative differential photometry in optical (Bessell) *R*band was obtained on 2014 April 23 and 24 with the automated and remotely controlled 0.4 m $f/8$ Cassegrain telescope, equipped with an SBIG ST10XME CCD camera and an $f/6.3$ focal reducer, at the University of Athens Observatory. The flare was observed from T0+8164 s to T0+21412 s and then again from T0+75155 s to T0+91971 s. The first 22 observations were removed due to light clouds, which affected the photometry. The cadence varied between 45 and 95 s, and relative flux measurements were made using nearby comparison stars. Additional observations in optical (Bessell) *B* and *R*bands were also obtained on 2014 August 4 and 5, to confirm the quiescent level. Raw images were corrected for dark current and reduced using sky-flat images. The aperture photometry package Munipack (Chrastina & Hroch 2008) was used for data reduction and extraction of magnitudes and errors. The resultant light curve is shown in Figure 1.

2.5. Photometry from the Upice Observatory

The remotely controlled telescope at the Upice Observatory in the Czech Republic was used to observe the field of DG CVn with a 20 cm Newtonian telescope, and SBIG CCD camera using *BVI* filters for photometry. Observations commenced 900 s after the initial trigger in the case of *V* filter observations, and spanned 4.3 hr. Additional observations over the following nights—three additional nights in the case of the *B* filter and about three weeks for the *V* filter—were also obtained to examine long timescale variability. The cadence of observations in *B* filter on the first day was about 30 s, increasing to 80 s on subsequent days, and for the *V* filter the corresponding cadences were about 60 s on the first day and 126–195 s on subsequent days. Raw images were corrected for dark current and the field was reduced using flat-field images combined from many images obtained during various sessions to get the resultant flat background. The aperture photometry package Munipack (Chrastina & Hroch 2008) was used for data reduction and extraction of magnitudes and errors. Data are shown in Figure 1.

2.6. Photometry from the Observatorio del CIECEM

Data on the first night were obtained with two 14 inch Schmidt–Cassegrain telescopes (one for *V*-band observations and the other for *B*-band) of the Observatorio del CIECEM in Huelva, Spain. The *V*-filter observations began starting at T0 +10173 s and lasted 3.8 hr; *B*-filter observations commenced 15610 s after the trigger, and spanned 2.3 hr. The observing cadence for the *V* filter data was about 20 s on the first day, with occasional longer cadences due to individual bad data

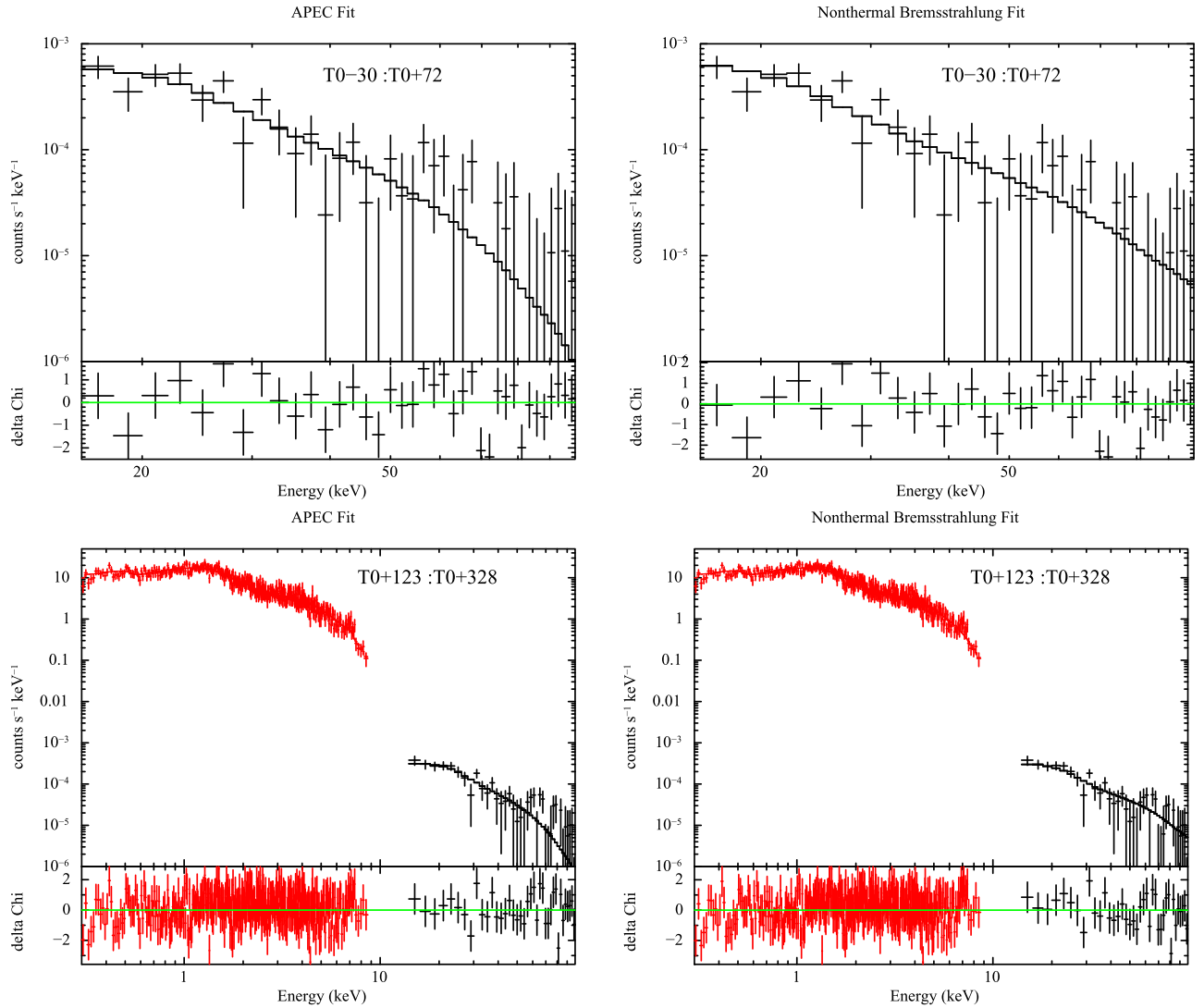

Figure 2. X-ray spectra at the time of the trigger (top panels, BAT only) and during the initial ∼200 s after the XRT and BAT both were on source (bottom panels). The left panels show spectra fit with thermal models; right panels show the same spectra fit with nonthermal models. Spectral fit parameters are given in Table 1.

points. Observations proceeded over the next five days, spanning about 2 hr on each of the next nights. Observations on these subsequent nights utilized a single 11 inch Schmidt–Cassegrain telescope, by alternating *V* and *B* filters in the time series. An exposure time of 30 s was used for the *V* band data, and 40 s for *B* band. Data are shown in Figure 1. In combining data from different telescopes using the same filter, we find calibration differences to be negligible.

3. DATA ANALYSIS

In addition to the multi-wavelength data presented in this paper, we also make use of radio data presented in Fender et al. (2015), and the *V* band photometry prior to the *Swift* trigger presented in Caballero-García et al. (2015). In this paper, we concentrate on the two main events evident in Figure 1: the big first flare (BFF), which appears to extend from T–40 s based on the timing reported in Caballero-García et al. (2015) until possibly later than T+328, when *Swift* ceased monitoring; and F2, whose peak is at about T0+10^4 s. Given the amplitudes, durations, and multi-wavelength data for these two events, there is much more that we can say about them.

3.1. X-Ray Spectra

3.1.1. Trigger and XRT+BAT Spectra of BFF

We fit the spectra obtained from the time intervals T0−30: T0+72 and T0+123:T0+328 from the BAT only (first interval) and XRT+BAT (second interval), using either a single temperature APEC (Astrophysical Plasma Emission Code) model or a nonthermal thick-target bremsstrahlung model. The amount of interstellar absorption was fixed to an N_H value of 4.7×10^{17} cm^{-2}, based on Mg II and Fe II column densities measured by Malamut et al. (2014) toward β Com, a star ∼4.°5 away in angular extent and with a proximity of 9 pc (S. Redfield 2016, private communication). APEC describes a collisionally ionized plasma in coronal equilibrium, with line emission formed predominantly from a balance of collisional excitations populating excited ionic states, and radiative de-excitations; this is the usual assumption for stellar coronal plasmas. We use a custom version of ATOMDB (Smith et al. 2001) calculated out to 100 keV[19], since the standard

[19] Available at http://www.atomdb.org/download_process.php?fname=atomdb_v2_0_2_runs.

Table 1
Spectral Fit Parameters for Trigger and Initial Decay of Flares on DG CVn

Parameter	T0−30:T0+72 BAT only	T0+123:T0+328[a] XRT+BAT
Thermal Fit		
T_X (10^6 K)	278^{+140}_{-92}	290 ± 31
$\mathcal{VEM}$ (10^{54} cm^{-3})	$9^{+4.7}_{-2.7}$	4.9 ± 0.1
χ^2 (dof)	38.2 (36)	401.6 (432)
f_X (14–100 keV) × 10^{-9} (erg cm^{-2} s^{-1})	$3.6^{+0.2}_{-0.8}$	$2.03^{+0.18}_{-0.15}$
f_X (0.3–10 keV) × 10^{-9} (erg cm^{-2} s^{-1})	(4.5)[b]	2.38 ± 0.03
f_X (0.01–100 keV) × 10^{-9} (erg cm^{-2} s^{-1})	9.3	5.1
Nonthermal Fit		
δ_X	3.6 ± 0.4	$3.2^{+0.2}_{-0.1}$
Power (10^{37} erg s^{-1})	$3^{+1.2}_{-1.1}$	1.11 ± 0.03
χ^2 (dof)	40.2 (36)	409.62 (432)
f_X (14–100 keV) × 10^{-9} (erg cm^{-2}s^{-1})	$3.8^{+0.2}_{-0.4}$	$2.24^{+0.19}_{-0.15}$
f_X (0.3–10 keV) × 10^{-9} (erg cm^{-2} s^{-1})	(5.8)[b]	$2.34^{+0.03}_{-0.02}$
f_X (0.01–100 keV) × 10^{-9} (erg cm^{-2} s^{-1})	11.	5.3

Notes.
[a] N_H fixed at 4.7 × 10^{17} cm^{-2}.
[b] Flux extrapolated from best-fit model in the 14–100 keV range.

ATOMDB energy grid delivered with XSPEC ends at 50 keV. The Volume Emission Measure ($\mathcal{VEM}$) quantifies the amount of plasma emitting at the fitted temperature, and is equivalent to $\int n_e^2 dV$. The nonthermal thick target model is often used to describe hard X-ray emission from solar flares. In this model, a power-law distribution of electrons with energy (described by the parameter δ_X) is modified by transport through a fully ionized plasma. From the observed spectrum, the index δ_X can be derived, as well as (for unresolved stellar observations) the power in the electron beam (see the discussion in Osten et al. 2007). In solar flare observations a broken power law is often observed, with low-energy cutoff (E_0) around 20 keV; in this case, we consider a single power law, with E_0 fixed to be 20 keV. The power required depends on the low-energy cutoff as $(20/E_0)^{(\delta_X-2)}$ as described in Osten et al. (2007), so decreasing the low-energy cutoff from 20 to 10 keV results in roughly a factor of two more power required for $\delta_X \sim 3$. The spectra are shown in Figure 2 and fit parameters are listed in Table 1. The 0.01–100 keV flux extrapolated from the best-fit model is also reported in Table 1. The two models are statistically indistinguishable for the same time interval.

The thermal fit shows that the spectrum from 0.3 to 100 keV for each time interval is dominated by a single temperature. Attempts to use a more complicated model, like multiple temperature components, did not result in a statistically better fit, demonstrating the dominance of the hot temperature plasma. We confirmed that the spectrum is dominated by the continuum from such a hot plasma by redoing the fit using a bremsstrahlung model (brems) in XSPEC, and comparing the result to the APEC fit. The bremsstrahlung model only includes contributions from H and He, which confirms the high-temperature results from fitting with APEC. There is no evidence for any lower temperature plasma, as evidenced by the lack of He- or H-like iron at characteristic energies of 6.7 and 6.9 keV.

Previous reports of stellar superflares with *Swift* had reported the detection of the Fe Kα line at 6.4 keV (Osten et al. 2007, 2010). However, these appear to be due to a calibration artifact unrecognized at the time, namely charge trapping (Pagani et al. 2011). The spectral fits to XRT data shown in Figures 2 for BFF and 3 for F2 do not show any evidence of excess emission near 6.4 keV.

3.1.2. XRT Spectra of F2

We extracted XRT spectra in four intervals during the peak and decay of the second large flare, F2. There was not enough signal in the BAT at this time to extract a spectrum, so we concentrate on the 0.3–10 keV range of the XRT. The four spectra were fit jointly, with a three temperature APEC model: the two lowest temperatures (corresponding to quiescent emission) were fixed to be the same for all four spectra, while the third temperature component corresponding to the flare emission was allowed to vary. We arrived at this after comparing the goodness-of-fit for models with different numbers of components. Values are given in Table 2. Columns labelled "Q1" and "Q2" list the results for the quiescent component; the metallicity was fixed to be unity (i.e., solar) for the spectral components. Spectral fits extracted for other times during the peak and decay of the flare are listed in separate columns. The temporal trends show a large temperature and volume emission measure at the earliest time interval, with generally decreasing plasma temperatures and volume emission measures during the decay of the flare. The abundance of the flaring plasma initially appears to be mildly sub-solar, but noise in the values fitted from spectra extracted at later times prevents the determination of a definitive trend. Since the spectra were fit together, a single value of the fit statistic was calculated: χ^2 of 749.81, with 787 degrees of freedom. Figure 3 shows the spectra along with the model fits. Table 2 also gives a flux extrapolated to the 0.01–100 keV range for intercomparison of the different time intervals and other flares.

3.2. Flaring Footpoint Emission.

We use the ground-based *V*-band, *R*-band, and *Swift*/UVOT data to determine the white-light emitting footpoint sizes during the peak of BFF and F2. We use the following equation to determine the fraction of the visible hemisphere, $X_{\rm flare} = R^2_{\rm flare}/R^2_\star$, producing white-light emission (Hawley et al. 2003)

$$\begin{aligned} F_{\rm flare,filter} &= I_{\rm f,filter} \times F_{\rm Q,filter} \\ &= X_{\rm flare,filter}\,(R^2_\star/d^2)\,\pi B_{\lambda=\lambda_{\rm eff}}(T_{\rm flare}) \end{aligned} \quad (1)$$

where $\pi R^2_{\rm flare}$ is the total flaring area, $F_{\rm flare,filter}$ is the observed peak flare flux in a particular filter, $I_{\rm f,filter}$ is the fractional increase relative to the quiescent flux during the flare, $F_{\rm Q,filter}$ is the quiescent flux in that filter, $B_{\lambda=\lambda_{\rm eff}}(T_{\rm flare})$ is the Planck function evaluated at the effective wavelength $\lambda_{\rm eff}$ of the filter, and $T_{\rm flare}$ is the temperature of the blackbody flare spectrum assumed to dominate the spectral energy distribution of the optical filter. The quantities $R_\star$ and d are the radius of the star

Table 2
Spectral Fit Parameters During F2 Event on DG CVn

Parameter	Q1	Q2	T0+10860:T0+11849	T0+16496:T0+17605	T0+22437:T0+23367	T0+28019:T0+29125
T_X (10^6 K)	$5.0^{+2.4}_{-1.3}$	$14.7^{+2.7}_{-2.8}$	$53.8^{+2.9}_{-3.8}$	$41.5^{+4.9}_{-4.4}$	$55.7^{+20.2}_{-13.0}$	$36.2^{+11.3}_{-7.8}$
$\mathcal{VEM}$ (10^{52} cm^{-3})	$1.3^{+0.8}_{-0.6}$	$3.6^{+2.3}_{-2.0}$	$154.9^{+5.5}_{-6.3}$	$105.3^{+8.6}_{-9.0}$	$38.6^{+8.3}_{-11.2}$	$43.0^{+8.2}_{-8.6}$
Z	1 (fixed)	1 (fixed)	$0.4^{+0.12}_{-0.12}$	$0.51^{+0.24}_{-0.20}$	$1.18^{+2.12}_{-0.88}$	$0.05^{+0.52}_{-0.05}$
f_X[a] (0.3–10 keV) $\times 10^{-10}$ (erg cm^{-2} s^{-1})	*0.09*[b]	*0.20*[b]	$6.59^{+0.07}_{-0.11}$	$4.35^{+0.11}_{-0.11}$	$2.26^{+0.10}_{-0.19}$	$1.60^{+0.14}_{-0.06}$
f_X[c] (0.01–100 keV) $\times 10^{-10}$ (erg cm^{-2} s^{-1})	*0.13*	*0.28*	*8.0*	*5.3*	*2.8*	*2.0*

Notes.
[a] Flux calculated for flaring time intervals includes contribution from the quiescent plasma component.
[b] Quiescent flux in this energy range calculated using best-fit model parameters.
[c] Flux extrapolated into this energy range using best-fit model parameters.

and its distance from Earth, respectively. We use this equation initially to calculate $X_{\rm flare,filter}$ for the peaks of both BFF and F2, assuming a $T = 10^4$ K blackbody flare spectrum, which is a reasonable approximation to the peak broadband color distribution during very large flares (Hawley & Fisher 1992). Riedel et al. (2014) list the *V*-band magnitude of the DG CVn system as $V = 12.02$, which we take as the quiescent value per star. We assume that both stars contribute equally to the brightness, so the quiescent *V*-band flux is 2.87×10^{-14} erg cm^{-2} s^{-1} Å^{-1}. We take the quiescent flux to be 5.4×10^{-14} erg cm^{-2} s^{-1} Å^{-1} for the *R*-band and 2.9×10^{-14} erg cm^{-2} s^{-1} Å^{-1} for the *Swift v*. We use the average of *uvw2* fluxes at t−T0 $> 1.3 \times 10^6$ s to determine the quiescent flux for *uvw2*. All values of I_f were calculated relative to one star, assuming the quiescent flux from the system can be divided equally between the two components). The peak *V*-band magnitude increase for BFF is $\Delta V = -5$ mag from Caballero-García et al. (2015), so the relative flux increase for one star is $I_{f,\ V} \sim 190$, whereas the *v*-band from *Swift* in the decay phase was at $I_{f,v} = 23.5$ at *T*0+113.5 s. For the *Swift v* measurement of BFF, there is an uncertainty of 0.21 mag due to saturation and spillover, so the measurement and uncertainty in $X_{\rm flare,filter}$ give $X_{{\rm BFF},v} \sim 0.044$ (0.035–0.054). The first *v*-band point from *Swift* is consistent with the *V*-band photometry from Caballero-García et al. (2015) in the decay phase of BFF. For F2, $I_{f,\ V} = 11.8$ at the flare peak, and $I_{f,uvw2} = 156$. These lead to $X_{{\rm BFF},V}(10^4\ {\rm K}) = 0.375$ for BFF and $X_{{\rm F2},V}(10^4\ {\rm K}) = 0.023$ for F2 based on *V*-band measurements. In the *R* band, $I_{f,\ R} = 5.9$ at the peak of F2 ($T0 + 9590$ s), leading to a value of $X_{{\rm F2},R}(10^4\ {\rm K}) = 0.031$. These values are summarized in Table 3. These footpoint sizes are extraordinary for M dwarf flares and are comparable to those inferred during the flares from Osten et al. (2010) and Schmidt et al. (2014), but 10 times larger than the peak footpoint sizes in the Great Flare on AD Leo (Hawley & Pettersen 1991, hereafter, HP91).

While a $T = 10^4$ K blackbody is reasonable for the impulsive phase of very large flares, the flare (F2) exhibits much longer timescales than BFF and may also exhibit different heating properties (e.g., through the appearance of a Vega-like spectrum; K13). Thus, we search for evidence of a different color temperature using the *V*- and *R*-band data during F2. The right panel of Figure 4 displays the V/R ratio during the decay phase of F2 in addition to the detailed *V* and *R* light curves, and reveals a ratio with a maximum value near 1.2 at the time of the peak of F2. A V/R ratio of ∼1 was also observed in the Great Flare on AD Leo[20] in the gradual phase (HP91) and a V/R ratio ∼1 was synthesized from spectra during the decay of the Megaflare on YZ CMi (Kowalski et al. 2010). The V/R ratio indicates a lower blackbody temperature, of about 6000 K, for F2, and we also calculate the $X_{\rm flare}$ values for this temperature as well in Table 3. Additional contributions from Balmer continuum emission are expected in the *Swift*/UVOT filter bandpasses (see the discussion in Kowalski et al. 2010) and a redder continuum component, termed "Conundruum" in Kowalski et al. (2013; hereafter K13), is also expected in the *R*-band. The broadband UVOT and *R*-band distribution will be discussed in more detail in future work (A. Kowalski et al. 2016, in preparation). The V/R color declines to less than one in the decay of the F2 event, which indicates a "cooler" Conundruum component in F2 than in the Megaflare (closer to the color temperature of the Conundruum in the IF3 event from K13; Figure 31 of that paper). Without spectra, we cannot assess the detailed properties of the changes in the blue continuum for the newly formed flare emission and thus we do not know the area of the newly formed kernels. However, the *V*-band flux experiences a much larger relative increase (seven times compared to the previously decaying emission from the BFF at T0+∼5e3s in Figure 4) than the synthesized *V*-flux increase (1.5 times) in the secondary events following the Megaflare event. Therefore, we would expect that persistent hot spots with very blue spectra (either a spectrum like a blackbody with $T \sim 10{,}000$ K or a Vega-like spectrum as found in Kowalski et al. 2010) would have resulted in a much larger change in the V/R flux ratio for F2. If we assume a value of the *R*-band flux before F2 (such that V/R just before F2 is the same as the V/R in the decay at T0+17,000 s), we estimate that the color temperature of the newly formed emission ranges between 6000 and 8000 K, but nowhere near the V/R value (1.7) for a Vega-like spectrum. The V/R color temperature of about 6000 K is evidence that increased Conundruum continuum emission dominates the optical brightness increase in the F2 event.

The *Swift uvw2* point, which falls near the peak of F2, but shortly afterward, can place some constraints on the relative contribution of blackbody versus Balmer continuum expected at these short wavelengths. No extinction correction has been applied here, but due to the proximity of the star and its

[20] *R* in this flare was obtained in Johnson *R*, which is redder and wider than Bessell R.

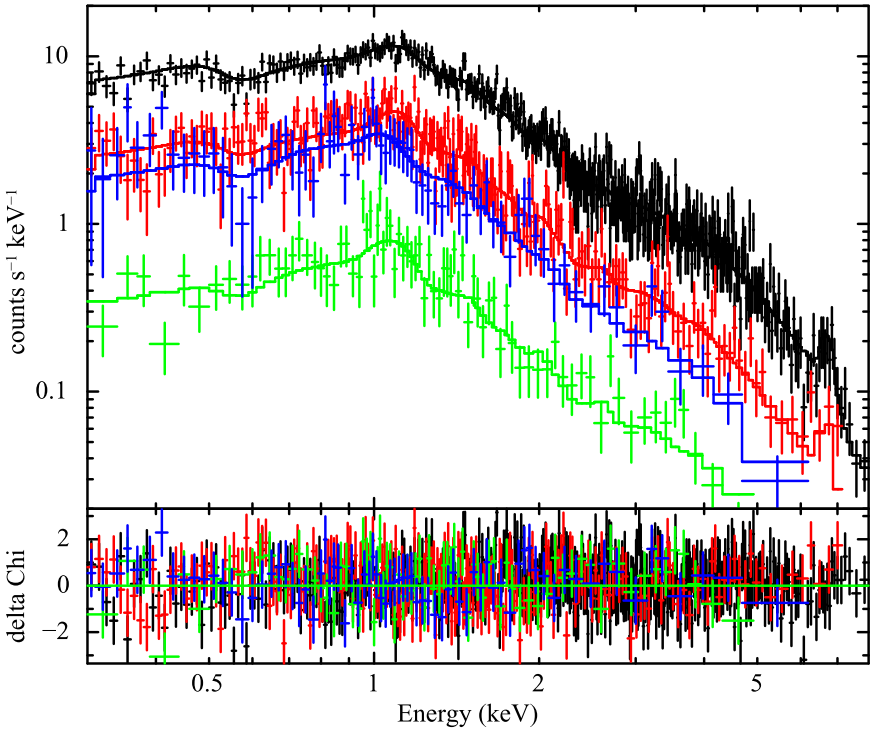

Figure 3. Top panel shows four spectra from the F2 event: black is T0+10860:T0+11849, red is T0+16496:T0+17605, green is T0+22437:T0+23367, and blue is T0+28019:T0+29125. Solid histogram gives the best-fit spectral model for that time interval; parameters are listed in Table 2. Bottom panel gives the contribution to the χ^2 statistic in each energy bin, for each data set and model.

Table 3
Implied Flaring Footpoint Area Fractions

Time (s)	Filter	I_f	$T_{\rm BB}$ (K)	$X_{\rm flare}$
		BFF		
T0–40	*V*	190	10^4	0.375
T0+113.5	*v*	23.5	10^4	0.044 (0.035–0.054)
		F2		
T0+9590	*R*	5.9	10^4	0.031
T0+9590	*R*	5.9	6000	0.15
T0+9710	*V*	11.8	10^4	0.023
T0+9710	*V*	11.8	6000	0.14
T0+11761	*uvw2*	156	10^4	0.005
T0+11761	*uvw2*	156	6000	0.59
T0+11753	*V*	5.1	10^4	0.01
T0+11753	*V*	5.1	6000	0.064

location out of the Galactic plane this will be negligible. At T0 +11753 to T0+11761, the flux ratio of $uvw2/V$ is $1.2 \times 10^{-13}/1.5 \times 10^{-13} = 0.8$. At T0+16951, the ratio of $uvw2/V$ is $4.2 \times 10^{-13}/4.6 \times 10^{-13} = 0.9$. It is interesting that $X_{\rm F2,\,uvw2}(T = 6000\ {\rm K})$ is 0.59 for *uvw2* and $X_{\rm F2,\ V} = 0.06$ for *V* at T0+11753 (see Table 3). This indicates that 10 times more emission is needed to account for the flux in the *uvw2* bandpass if a 6000 K blackbody (or any spectrum that is of similar shape as a 6000 K blackbody) is extrapolated to $\lambda = 2030$ Å. In the impulsive beam heating phase of the F11, F12, and F13 models from Kowalski et al. (2015), the average values of the continuum flux ratio 2030/5500 Å are 1.8, 2.0, and 3.1 for these models respectively. So a ratio of 0.8–0.9 (even given a 20% uncertainty from comparing satellite and ground-based broadband data) can be used as a strong constraint on heating models. If the 6000 K blackbody is a good approximation to the *V* and *R* continuum in the F2 event, then there is Balmer continuum necessary to account for the *uvw2* data point, but not as much Balmer continuum as the impulsive phase F11 or F12 models predict.

The Megaflare described by K13 was similar to the situation presented here in that a second large flare occurred during the decay phase of a large, $\Delta U = -6$ mag, flare brightening on the nearby flare star YZ CMi. While the YZ CMi events did not have coverage by high-energy satellites, they did have comprehensive blue-optical spectrophotometric coverage, which enabled several inferences to be drawn about the behavior of the lower stellar atmosphere. Spectra covering the green and red continuum ($\lambda > 5000$ Å) in the Megaflare indicate the presence of a significant red continuum component with $T_{\rm BB} \approx 5500$ K (Figure 31 of K13). At the same time, the blue continuum ($\lambda = 4000$–4800 Å) exhibited a hotter (~8000–8500 K) color temperature than in the red. During the secondary flares in the decay phase of the Megaflare, the blue continuum increased in color temperature to 11,000 K (Table 9, K13), which was attributed to newly formed flare emission resembling the spectrum of Vega. Over the secondary flares, the V/R ratio changed from 1.0 to 1.1 indicating that the broad continuum covering the *V* and *R* bands remained relatively flat, due to the brightness of the decay emission that was dominated by the Conundruum continuum component. The appearance of a very blue spectrum ($T_{\rm BB} \sim 15{,}000$ K; Table 9 of K13) in these secondary flares had a small effect on the V/R value of the total (decay + secondary flare) emission.

Invoking the solar analogy of a two ribbon flare, which was applied to the Megaflare (Kowalski et al. 2012), the

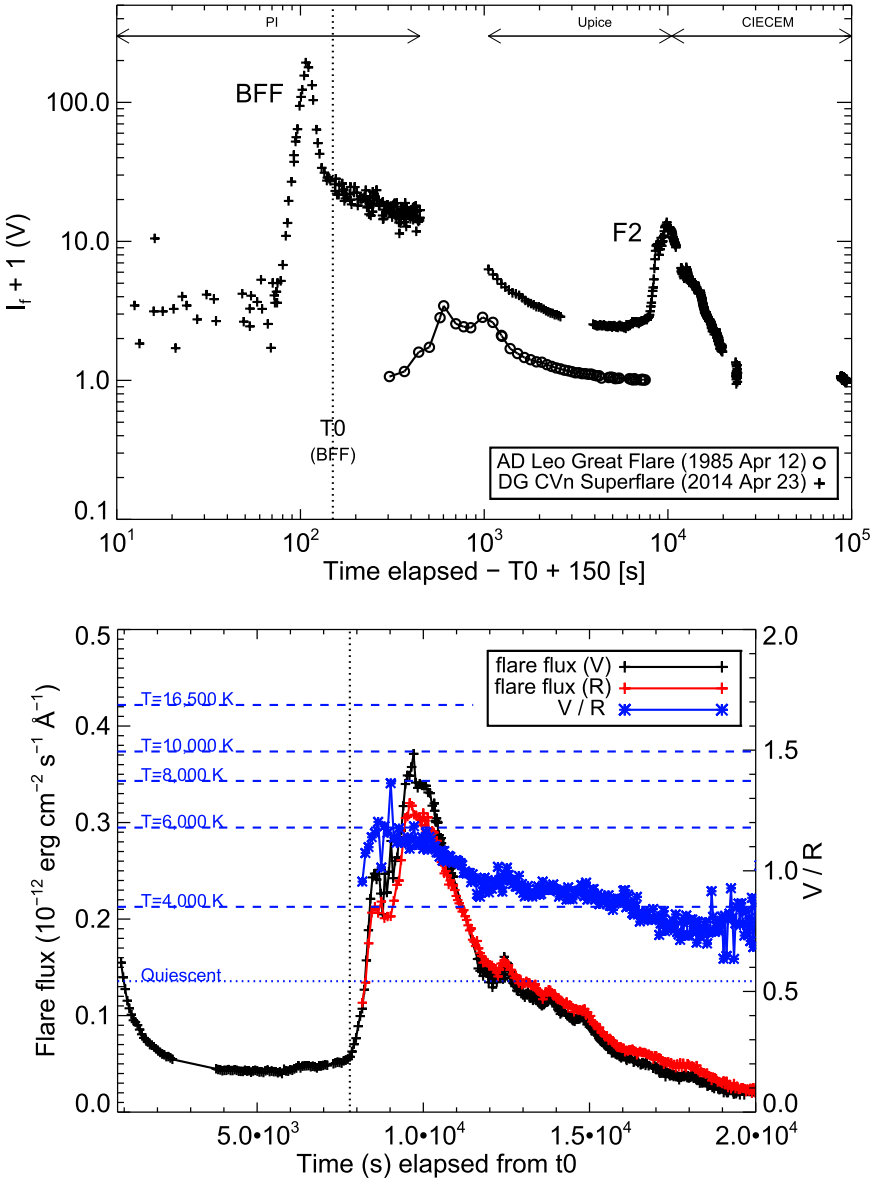

Figure 4. (Top) plot of fractional increase relative to quiescent flux in the *V* band for DG CVn showing both BFF and F2 events, along with AD Leo Great Flare described in HP91 for comparison. The disparity in timescales between BFF, with an FHWM of 20 s, and F2, with an FWHM of 3600 s, is apparent. (Bottom) comparison of *R*- and *V*-band light curves of the F2 event, along with flux ratio. Blue dashed lines indicate the approximate value of the V/R ratio expected for a flare spectral energy distribution dominated by a blackbody with the temperatures listed.

relevant flaring areas for the DG CVn superflare are the following.

1. The area of the decaying emission before F2 occurred. This area could be decaying ribbon emission from the BFF event, and is likely dominated by Conundruum continuum emission and Balmer continuum emission (where the area fractions occupied by these two components are roughly equal). Or it could be decaying emission from loops ignited at earlier times in F2.
2. The area of newly formed flare emission during the F2 event. This area is white-light kernel emission at the footpoints of newly reconnected flare loops. This may be an area of hot blackbody-like emitting kernels with X_{F2} ($T \sim 10{,}000$ K), but we do not have flux-calibrated blue spectra to characterize the color temperature from $\lambda = 4000$–4800 Å.

It is possible that the lifetime of the hot blackbody emission in each newly formed flare kernel is much less than the F2 event duration of ∼3600 s and thus the blue spectra from each burst decay quickly leaving bright Conundruum emission to dominate the flare energy over a long timescale. To obtain a flare footpoint area, we assume the following: (1) the area of the newly formed flare emission is approximately equal to the area of the Conundruum continuum emission (however, the loops producing Conundruum and loops producing hot blackbody emission may have different heating sources); (2) the Conundruum emission can be approximated by blackbody radiation (the emissivity process(es) that give rise to the Conundruum emission are not yet well understood; see K13); (3) the Hα, He I 5876, and Na I D line contributions to the *R* band are small relative to the continuum (at most 10% is attributed to Hα in the gradual phase of other large flares;

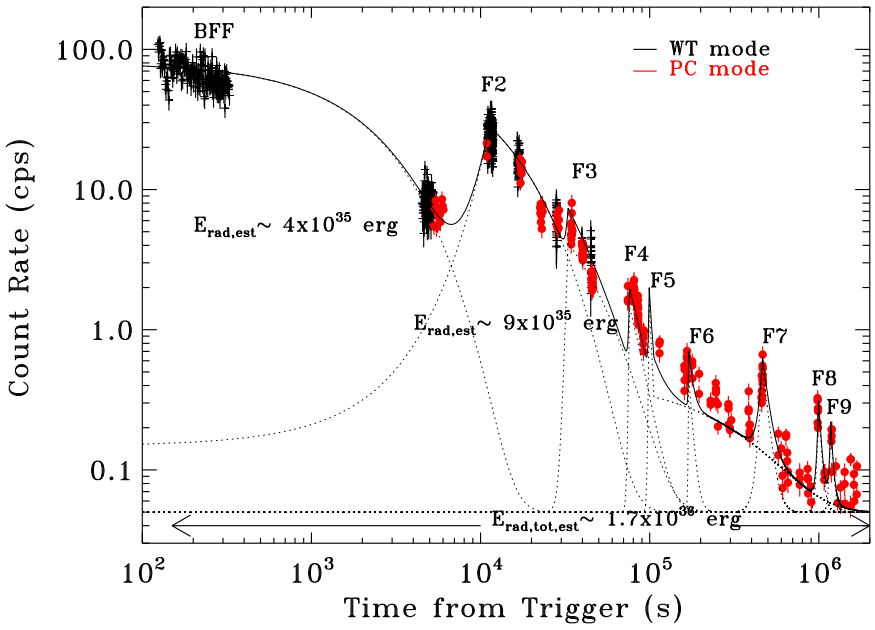

Figure 5. *Swift* XRT light curve of the coverage of the initial trigger and subsequent flaring activity of DG CVn over the following ~21 days. Because of gaps in the data, exponential rises and decays were used to approximate the observed behavior, and the models were integrated in time to estimate flare radiated energies in the 0.3–10 keV bandpass.

HP1991 and K13). Using $T \sim 6000$ K, for the peak of F2, we use the V/R band ratio to determine that $X_{\rm flare} = X_{\rm Conundruum} = 0.14$ (see Table 3). The density of the plasma producing the Conundruum should be investigated with radiative-hydrodynamic "multithread" models.

3.3. Energetics

3.3.1. X-Ray Radiated Energy

Calculation of the X-ray radiated energy is made difficult by data gaps arising from satellite occultations, as well as limitations of data from the BAT due to signal-to-noise constraints. We attempt to account for the energetics in a couple of ways, to estimate the total energy for BFF and F2. Table 1 lists the fluxes in two intervals of time for which flux measurements in the 14–100 keV bandpass can be made; for one of these time intervals, the flux in the 0.3–10 keV interval can be measured directly, and in the other it can be estimated by extrapolating the best-fit spectral model into this energy region. Because of the data gaps, we could not perform direct integration under the X-ray light curve. Instead, we assumed continuity of the flares across the data gaps and used exponential rises and decays to parameterize the light curve as a series of flare events; the parameters were not fit to the light curve, but rather were varied to approximate the shape of the light curve. Figure 5 shows the XRT light curve with these fits. Thus the energy estimate done this way is only approximate. We note that the radio light curve in Fender et al. (2015) shows the radio flare decay of BFF in the *Swift* data gap, showing its decay to be relatively simple. We used energy conversion factors from the spectral modeling described above to determine the integrated energy in the 0.3–10 keV bandpass. This gives an estimated X-ray radiated energy for BFF in the 0.3–10 keV range, from T0+123 to approximately T0+10^4 s, of 4 × 10^{35} erg. We can add in the radiated energy in the 14–100 keV bandpass from T0−30:T0+328, using the fluxes derived from spectral modeling in Table 1, and the 0.3–10 keV flux in the T0−30:T0+72 time range listed in Table 1 and extrapolated from the best-fit model to the 14–100 keV energy range. These last two contributions are ≈5 × 10^{34} erg, putting a lower limit on the X-ray radiated energy in the 0.01–100 keV range for BFF of ≈4.5 × 10^{35} erg. We also calculate an upper limit to the energy radiated in the 0.01–100 keV bandpass by using the ratio of flux in the 0.01–100 keV energy range to that in the 0.3–10 keV range, as listed in Table 1 for BFF. For BFF, the ratio for both time intervals in Table 1 is ~2, so the radiated energy in the 0.01–100 keV bandpass could be as much as twice that deduced from the 0.3 to 10 keV energy range, or 8 × 10^{35} erg. We take the duration of BFF to be the time from the optical rise preceding the trigger, occuring around T0–70 s as discussed in Caballero-García et al. (2015), until the transition from BFF to F2 in the optical light curves, at around T0+7750 s.

The F2 event is considerably longer-lasting than BFF, extending from about T0+6800 to about T0+30800 s. The decay could be even longer; because of the decrease in count rate and shorter monitoring intervals it is difficult to see whether the behavior from about 2–5 × 10^4 s is a continuing decay from the peak of F2 or whether there are subsequent smaller flares occurring. The spectral fitting for this event, in Section 3.1.2, does suggest that the plasma is cooling. The radiated energy in the 0.3–10 keV band for the F2 event is 9 × 10^{35} erg, more than twice the already large energy of BFF; this is due primarily to the extended duration of F2, as its count rate is lower. Calculating an upper limit for the energy radiated in the 0.01–100 keV bandpass, using the ratio of flux in the 0.01–100 keV energy range to the 0.3–10 keV range, we find that the ratio for F2 peaks at 1.2 for the first time interval in the flare, and decreases thereafter. This implies a correction of at most 20% in the radiated energy determined for the 0.3–10 keV bandpass, or a 0.01–100 keV radiated energy of 10^{36} erg. We take the duration of F2 to be approximately the interval T0 +6800:T0+30800 s.

The radio data also reveal the presence of a radio flare at ∼1 day, which falls in a gap of the X-ray data. We accounted for this "missing" flare using an approximate rise and decay that would fit within the gap in the X-ray data (named F5). Accounting for the several smaller events that occurred afterward, we estimate the total radiated X-ray energy for the series of events spanning ∼19 days to be about 2×10^{36} erg. We note that this is only an approximation, due to the data gaps, but it suggests that F2 was responsible for about half of the energy release during this extended period, with BFF responsible for half as much X-ray radiated energy.

3.3.2. R-band Radiated Energy.

The *R*-band light curve of F2 peaks at T0+9590 s and has a duration of 3.62 hr (from T0+8165 to T0+21,200 s). At the beginning of the *R*-band observations, DG CVn was already 0.78 mag brighter than quiescence, and was increasing in brightness. The observed duration of the rise phase is 1300 s, and at the peak of F2, the system is 1.49 mag brighter than quiescence. The flare energy is the quiescent luminosity multiplied by the equivalent duration of the flare (Gershberg 1972). The equivalent duration (of one star) for F2 is 2.84×10^4 s, giving an *R*-band flare energy of $E_{\mathrm{F2},R} = 8.5 \times 10^{34}$ erg. Figure 4 shows the *V*-band flare light curve, along with that of the "great flare" of AD Leo from HP91 for perspective.

3.3.3. V-band Radiated Energy

V-band light curves are available for both BFF and F2: the former from Caballero-García et al. (2015), and the latter in this paper. From inspection of Figure 1 of Caballero-García et al. (2015), it is clear that the system was slightly elevated at the start of their optical data, before the burst beginning around t −T0 = −70 s, which corresponds to BFF. The disparity in timescales in the *V* band between BFF and F2 is apparent in Figure 4, with an FWHM duration of 20 s for BFF, and ∼3600 s for F2. We translated the light-curve data from Caballero-García et al.'s (2015) Figure 1, using GraphClick, to estimate what the integrated *V*-band energy of BFF might be, in combination with *V*-band measurements presented here, which reveal the light-curve behavior just prior to F2. This corresponds to an integrated energy in the *V* band of about 2.8×10^{34} erg for BFF, from T0–146 to T0+7730.

We estimate the *V*-band radiated energy for F2 using direct integration from the light curve. From T0+7730 to T0+23754, the integrated energy is 5.2×10^{34} erg. The light-curve behavior in Figure 1 for the *V* band appears to demonstrate that the system has returned to its quiescent value after F2, though the gaps in the photometry prevent a definitive statement. The impulsive phase initiation of F2 is obvious from the light curve, though the decay from BFF flattened out for a long time before this, being ∼0.6 mag above the quiescent system *V* magnitude. The fact that the *V* band photometry was also enhanced prior to the BFF burst at t−T0 = −70 s suggests that there may have been an even earlier event missed in all wavelengths.

3.3.4. Energy Partition in BFF and F2 and Estimates of Total Radiated Energy

Table 4 lists the X-ray and optical energies derived for both BFF and F2, as discussed in Sections 3.3.1–3.3.3. We have measurements of the X-ray and *V*-band energy for both events, as well as (for F2) radiated energy in the *R* band. F2 is the more energetic of the two events; there also appears to be a difference of about a factor of two in the energy of the two events in both the 0.3–10 keV X-ray band and *V*-band radiated energies. We estimate the *U*-band energy using E_U–E_V scalings from Hawley & Pettersen (1991). Although the X-ray radiated energy in the 0.3–10 keV band appears to differ only by about a factor of two for the two events, the high plasma temperatures derived for BFF increase the wavelength range over which significant emission is received. As discussed in Section 3.3.1, we can come up with a range of the likely coronal radiated energy by considering a wider photon energy range. Consideration of this wider wavelength range increases the amount of radiated energy from coronal plasma, up to the point where the coronal radiated energy from BFF is only slightly less than that from F2. This suggests that the energy partition in each event does not follow the same trend.

Table 4
Energy Partition in DG CVn BFF and F2 Events[a]

Filter/Bandpass	DG CVn BFF	DG CVn F2
X-ray (0.3–10 keV)	4×10^{35}	9×10^{35}
X-ray (0.01–100 keV)	$4.5 - \leqslant 8 \times 10^{35}$	$\leqslant 10^{36}$
V	2.8×10^{34}	5.2×10^{34}
R	…	8.5×10^{34}
U[b]	*4.7 × 10³⁴*	*8.8 × 10³⁴*
$E_{\mathrm{bol},U}$[c]	*4.2 × 10³⁵*	*8.0 × 10³⁵*
$E_{\mathrm{bol},X}$[d]	*1.3 × 10³⁶*	*3 × 10³⁶*

Notes.
[a] Unit for the energies is erg. Italicized numbers are derived; see Section 3.3.4 for details.
[b] *U* band energy derived from *V* band energy and E_U–E_V scaling of Hawley & Pettersen (1991).
[c] Bolometric radiated energy derived from estimated *U* band energy and E_U–E_{bol} scaling of Osten & Wolk (2015).
[d] Bolometric radiated energy derived from 0.3 to 10 keV X-ray energy and E_X–E_{bol} scaling of Osten & Wolk (2015).

Osten & Wolk (2015) described energy partition in solar and stellar flares using smaller stellar flares, and demonstrated a rough agreement between solar and stellar flares in the relative fraction of radiated energy appearing coronal plasma and that in the hot blackbody emission, which dominates the *U*-band. From their Table 2, we estimate the bolometric radiated energy two ways: using the extrapolated *U*-band energy described above, as well as the X-ray energies calculated in Section 3.3.1. The estimation of bolometric energy using the coronal radiated energy is imprecise because the formulation of Osten & Wolk (2015) only considered the 0.01–10 keV energy range, whereas the BFF event clearly has significant contribution at higher photon energies. The two estimates of bolometric energy differ from each other by a factor of three or more. If the same relative contribution does hold for all of the coronal plasma, then accounting for the upper limit to the total coronal radiated energy in the 0.01–100 keV for BFF suggests that BFF and F2 may have been comparably energetic, at a few $\times 10^{36}$ erg. The fact that the bolometric energy estimates generated each of two ways differ from each other by about a factor of three or so suggests that the energy partition is not constant from flare to flare. Considering the upper limits to X-ray radiated energy and the *V*-band radiated energy, the ratio varies from $E_X/E_V \approx 28$

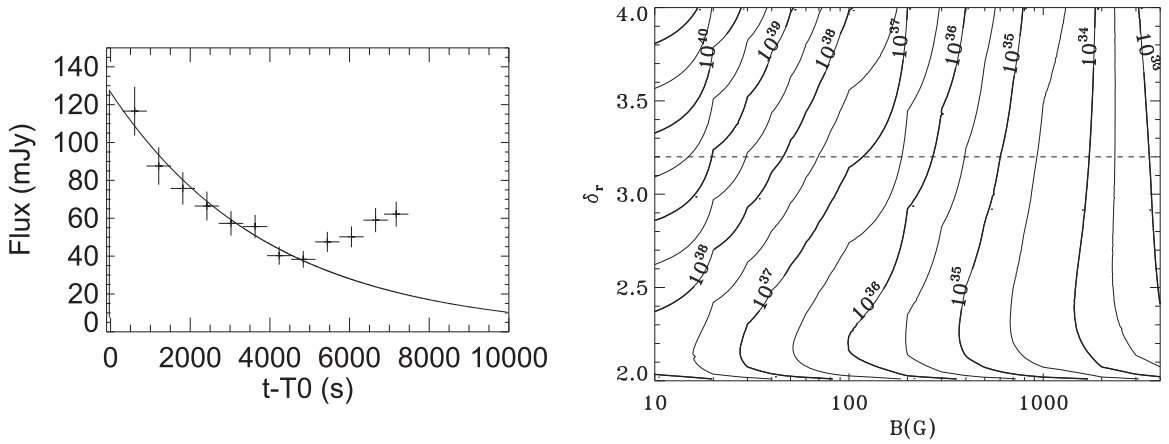

Figure 6. (Left) radio light curve of BFF, from Fender et al. (2015). Plusses indicate the temporal extent of each bin and the flux uncertainties. The main event is described as a linear rise and exponential decay, shown in the thick black line. (Right) dependence of kinetic energy in electrons on the index of the electron energy distribution δ_r and the magnetic field strength in the radio-emitting region B. Thick lines give values of the kinetic energy in powers of 10, and thin lines give the value at half-decade intervals. The dotted line shows the value of δ_X derived from fitting the X-ray spectra as nonthermal thick-target bremsstrahlung emission, from Section 3.1.1.

for BFF, and ≈20 for F2. The BFF event had significantly more coronal radiation than F2 when considered relative to the optical radiated energy. The data are too sparse to determine whether there is a relationship between the size of the flare or other parameters and the energy partition determined.

3.3.5. Kinetic Energy

Fender et al. (2015) presented 15.7 GHz data obtained starting about 6 minutes after the *Swift* trigger of DG CVn. Since the radio flare traces the action of nonthermal particles, these measures constrain the amount of kinetic energy in the BFF. We follow the treatment of Smith et al. (2005) in estimating the kinetic energy from the radio light curve. By assuming a spectral energy distribution of the radio emission, and modeling the temporal evolution of the emission, we can estimate the total radio energy, and hence the kinetic energy. The free parameters are the magnetic field strength in the radio-emitting source and the distribution of the accelerated electrons. The radio light-curve data is taken from Fender et al. (2015), and the portion within ∼2 hr of the trigger is shown in Figure 6; we use these data to constrain the time profile of the radio flare. Since the radio data suggest there was a single decline from the peak, we model the time profile of BFF as a single exponential decay, with a peak at the start time suggested from the start of the V band burst reported in Caballero-García et al. (2015), namely T0−70 s. We assume a fast linear rise to the maximum flux. The decay is fit from the radio light curve, and is 3980 s; we assume there is a single exponential decay during the decline of the radio flare. We also assume that the radio spectrum has a spectral shape of the form

$$S_\nu = A\nu^{\alpha_1} \text{ for } \nu \leqslant \nu_{\rm pk} \quad (2)$$

$$S_\nu = B\nu^{\alpha_2} \text{ for } \nu \geqslant \nu_{\rm pk} \quad (3)$$

where S_ν is the radio flux density, $\nu_{\rm pk}$ is the peak frequency, separating optically thick ($\nu \leqslant \nu_{\rm pk}$) emission with spectral index α_1 from optically thin ($\nu \geqslant \nu_{\rm pk}$) emission with spectral index α_2, and A and B are prefactors describing the dependence of the radio emission on other parameters. We assume that the peak frequency does not change during the decay, though there is evidence from solar and stellar flares that the peak frequency does change during the impulsive phase (Lee & Gary 2000; Osten et al. 2005). The spectral indices for a homogeneous radio-emitting source, on either side of $\nu_{\rm pk}$ are

$$\alpha_1 = 2.5 + 0.085\delta_r \quad (4)$$

$$\alpha_2 = 1.22 - 0.90\delta_r \quad (5)$$

(Dulk 1985), where δ_r is the index of the distribution of nonthermal electrons. The dependence of the number density of nonthermal electrons with energy and time, $n(E, t)$ is a separable function and has the form

$$n(E, t) = \frac{N(t)(\delta_r - 1)}{E_0}(E/E_0)^{-\delta_r} \quad (6)$$

where E is the electron energy, $N(t)$ describes the temporal behavior of the number of accelerated particles, and E_0 is a cutoff energy, usually taken to be 10 keV (Dulk 1985). Using this formalism, the time evolution seen at $\nu_{\rm AMI} = 15.7$ GHz, $F(t)$, can be applied to all frequencies

$$S(\nu, t) = F(t)\left(\frac{\nu}{\nu_{\rm AMI}}\right)^{\alpha_2} \text{ for } \nu \geqslant \nu_{\rm pk} \quad (7)$$

$$S(\nu, t) = \frac{(Ft)\nu_{\rm pk}^{(\alpha_2-\alpha_1)}}{\nu_{\rm AMI}^{\alpha_2}}\nu^{\alpha_1} \text{ for } \nu \leqslant \nu_{\rm pk} \quad (8)$$

where we have assumed $\nu_{\rm pk} < \nu_{\rm AMI}$. Solar and stellar radio observations show that the peak frequency $\nu_{\rm pk}$ is usually ∼10 GHz. Since DG CVn is at a known distance, we then convert this to $L_r(\nu, t)$ (erg s^{-1} Hz^{-1}) to describe the temporal and spectral behavior of the flare.

The kinetic energy at a given time is then determined by integrating over the energy dependence from the lower energy cutoff to infinity

$$E_{\rm kin}(t) = N(t)V(t)\frac{\delta_r - 1}{\delta_r - 2}E_0 \quad (9)$$

where $V(t)$ is the source volume. For optically thin emission the flux density can be expressed as

$$S(\nu, t) = k\nu^2/c^2 \int T_b(\nu, t)d\Omega(t) \quad (10)$$

$$= \frac{\eta(\nu, t) V(t)}{d^2} \quad (11)$$

where k is the Boltzmann's constant, c is the speed of light, T_b is the brightness temperature, and $d\Omega$ is the solid angle subtended by the radio-emitting source. The equation can be rewritten using $T_b = c^2/k/\nu^2\eta(\nu)L$ for $\tau_\nu \ll 1$, $\eta(\nu)$ is the gyrosynchrotron emissivity, L the length scale of radio-emitting material, and d the stellar distance. The radio luminosity can then be expressed as

$$L_r(\nu, t) = 4\pi\eta(\nu, t) V(t). \quad (12)$$

We use the analytic expressions for the emissivity η for X-mode emission from Dulk (1985)

$$\eta(\nu, t) = 3.3 \times 10^{-24} 10^{-0.52\delta_r} \times BN(t)(\sin\theta)^{-0.43+0.65\delta_r} \times \left(\frac{\nu}{\nu_B}\right)^{1.22-0.9\delta_r} \quad (13)$$

where B is the magnetic field strength in the radio-emitting source, θ is the angle between the radio-emitting region and the line of sight, and ν_B is the electron gyrofrequency. We define $A(\nu)$ to contain the constant and frequency-dependent prefactors, and substitute this into η

$$\eta(\nu, t) = A(\nu) N(t), \quad \text{with} \quad (14)$$

$$A(\nu) = 3.3 \times 10^{-24} 10^{-0.52\delta_r} \times B(\sin\theta)^{-0.43+0.65\delta_r} \times \left(\frac{\nu}{\nu_B}\right)^{1.22-0.9\delta_r} \quad (15)$$

where we are assuming that the magnetic field strength in the radio-emitting source does not change appreciably with time. Then, L_r can be expressed as

$$L_r(\nu, t) = 4\pi A(\nu) N(t) V(t). \quad (16)$$

This can be rearranged so that

$$N(t) V(t) = \frac{\int L_r(t, \nu) d\nu}{4\pi \int A(\nu d\nu)} \quad (17)$$

and

$$E_{\rm kin,tot} = \int N(t) V(t) \frac{\delta_r - 1}{\delta_r - 2} E_0 dt. \quad (18)$$

Particles will be depleted and replenished during this time; this can be accounted for in the temporal variations. The incompleteness of the observational data, coupled with some of the assumptions made in the analysis, will not render this a precise estimate of the kinetic energy, but does allow for an order of magnitude estimation, given the magnetic field strength in the radio-emitting source and a constraint on the energy distribution of accelerated particles. Since stellar radio data are usually consistent with a relatively hard radio spectra, we examine δ_r in the range of $2.2 \leqslant \delta_r \leqslant 3.9$. The right panel of Figure 6 shows the parametric dependence of the kinetic energy on the unknown values of magnetic field strength and index of the nonthermal electron distribution. The implied kinetic energy ranges from very large values, of $\sim 10^{40}$ erg for low values of magnetic field (tens of Gauss) and high values of δ_r, to 10^{34} erg and less for kiloGauss fields and a range of δ_r. These constraints will be used in Section 4.2 to aid in the constraint on the thermal or nonthermal nature of the X-ray emission in BFF.

3.4. Coronal Loop Length Determination

We used the method of Reale et al. (1997) to infer a loop length corresponding to the X-ray emission from the decaying phase of F2. As described in Osten et al. (2010) applied to *Swift* data, the thermodynamic loop decay time can be expressed (Serio et al. 1991) as

$$\tau_{\rm th} = \alpha l / \sqrt{T_{\rm max}} \quad (19)$$

where $\alpha = 3.7 \times 10^{-4}$ cm^{-1} s^{-1} K$^{1/2}$, l is the loop half-length in centimeters, and $T_{\rm max}$ is the flare maximum temperature (K),

$$T_{\rm max} = 0.0261 T_{\rm obs}^{1.244} \quad (20)$$

and $T_{\rm obs}$ is the maximum best-fit temperature derived from single temperature fitting of the data. The ratio of the observed exponential light-curve decay time $\tau_{\rm LC}$ to the thermodynamic decay time $\tau_{\rm th}$ can be written as a function that depends on the slope ζ of the decay in the $\log(n_e$–$T_e)$ plane (or equivalently, $\log(\sqrt{\mathcal{VEM}} - T)$ plane) and other parameters

$$\tau_{\rm LC}/\tau_{\rm th} = \frac{c_a}{\zeta - \zeta_a} + q_a = F(\zeta). \quad (21)$$

The parameters fit the functional form above and described in Reale et al. (1997); q_a, c_a, and ζ_a are determined for the *Swift*/XRT instrument to be $q_a = 0.67 \pm 0.33$, $c_a = 1.81 \pm 0.21$, and $\zeta_a = 0.1 \pm 0.05$ (F. Reale 2010, private communication). Combining the above expression with the one for the thermodynamic loop decay time, a relationship between flare maximum temperature, light-curve exponential decay time, and slope in the density–temperature plane can be used to estimate the flare half-length

$$l = \frac{\tau_{\rm LC}\sqrt{T_{\rm max}}}{\alpha F(\zeta)}, \quad (22)$$

valid for $0.4 \leqslant \zeta \leqslant 1.9$. The errors on plasma parameters quoted in Table 2 are 90% confidence intervals, whereas the uncertainties on q_a, c_a, and ζ_a are 1σ values, so we recomputed 1σ uncertainties for temperature and $\mathcal{VEM}$ to calculate ζ and coronal loop length in a consistent fashion.

Figure 7 shows T, $\mathcal{VEM}$ measurements of F2, from which we derive $\zeta = 0.45 \pm 0.20$. The right panel of Figure 7 shows the XRT light curve during the decay phase of F2, where an exponential decay time $\tau_{\rm LC}$ is determined to be 11122 ± 163 s. Combining these parameters with the value of $T_{\rm obs}$ from T0 +10860:T0+11849 in Table 2 and using Equation (22), the loop semi-length l is $5.4 \pm 2.9 \times 10^{10}$ cm, or 2.0 ± 1.0 stellar radii. Assuming a circular loop, this suggests a height above the photosphere of $2l/\pi$ or $1.3 \pm 0.6\ R_\star$.

4. DISCUSSION

The F2 event seems like a typical example of a superflare: hot plasma is produced and footpoint emission occurs, displaying the response of the upper stellar atmosphere (the X-ray-emitting corona) as well as the stellar photosphere (optical photometry) to the deposition of energy from presumably a magnetic reconnection event. The coronal loop

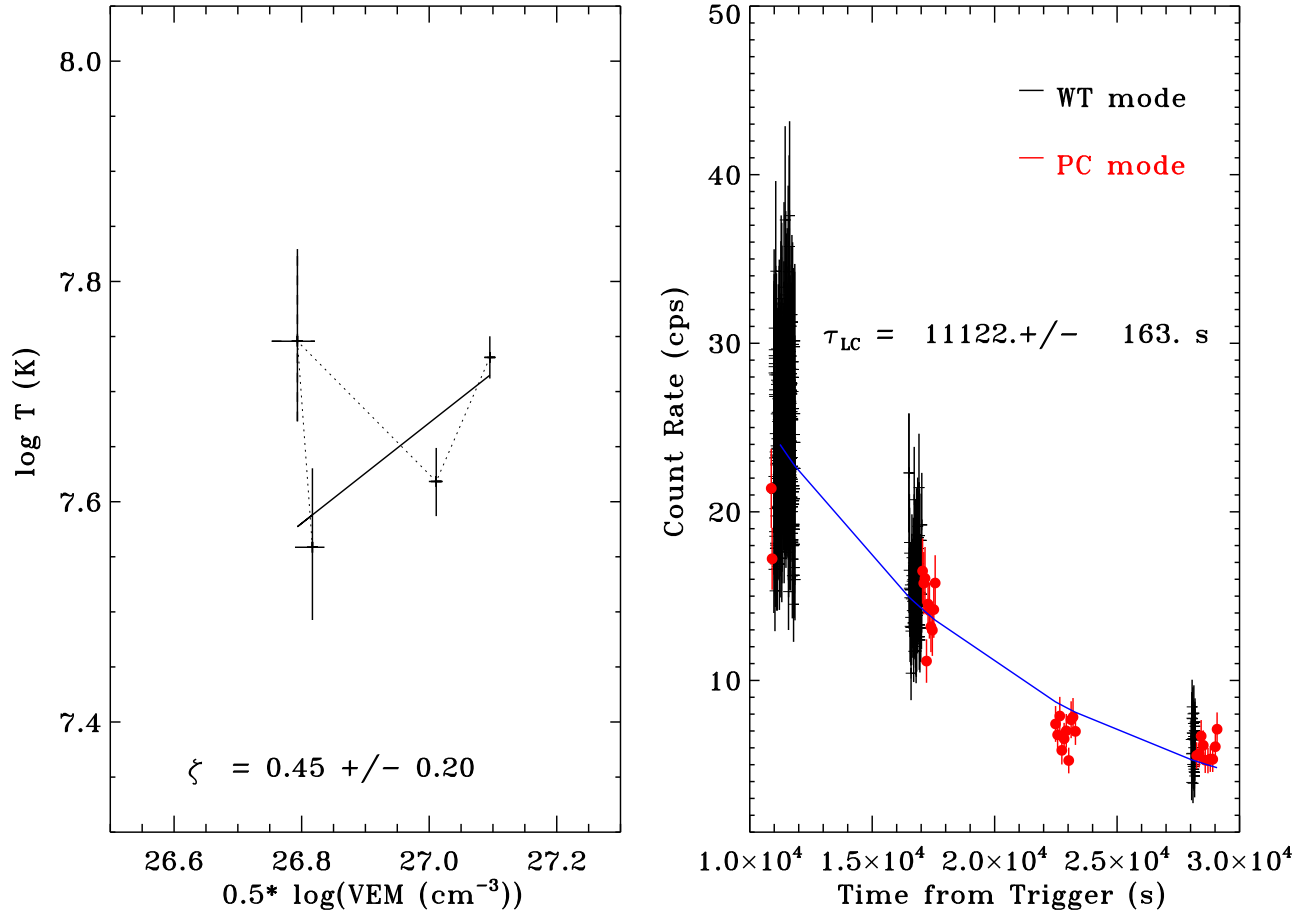

Figure 7. (Left) The trend of temperature vs. the square root of volume emission measure derived from each spectrum, for the F2 event, along with a determination of the slope ζ, given by the solid line. Dotted line connects data points in temporal order, starting from the upper rightmost point. One-σ error bars on temperature and $\mathcal{VEM}$ are used in the analysis. (Right) Decay time of F2 from light curve.

lengths implied by an analysis of the decay phase of F2 are in line with results from other large stellar flares, which have displayed loop semi-lengths up to 10^{12} cm on young stars (Favata et al. 2005; McCleary & Wolk 2011). The interpretation of BFF is more complicated because the X-ray spectra show the dominance of either a superhot thermal plasma component or nonthermal X-ray emission. Both of these possibilities are extreme. The former would be the hottest spectroscopically confirmed plasma temperature in a stellar flare, outstripping the $T_X \sim 100$ MK seen in other superflares (Osten et al. 2007, 2010). There is only one other claim on nonthermal hard X-ray emission in a stellar superflare, that of Osten et al. (2007). Given the close proximity in time of F2 and BFF, possibly formed in the same AR, we examine the implications of the F2 event to see what it can tell us about BFF and ultimately, the nature of these extreme stellar superflares.

4.1. The F2 Event

The energetics of F2 in different bands were determined in Sections 3.3.1–3.3.3, estimate of the coronal loop length in Section 3.4, and optical footpoint area in Section 3.2. Using these pieces of information, along with other parameters estimated from spectroscopic analysis, we determine some other parameters for F2, which will be useful in comparison with BFF. These numbers are tabulated in Table 5.

For the F2 event, the relative energetics in the V and R filters compare favorably with the Great Flare on the nearby M dwarf AD Leo described by HP91, even though the overall energetics are about a factor of 20 higher. In that event, based on their Table 6, 1.8 times more energy was released in the R band compared to the V band. As described in Sections 3.3.2 and 3.3.3, approximately the same energy ratio is observed for F2. The X-ray energy for F2, estimated in Section 3.3.1, is an order of magnitude larger still. While this is a large number in consideration of the typical radiated flare energies from nearby M dwarfs, it is not out of line with extremes of activity seen in very young stars. Caramazza et al. (2007) studied X-ray flares on low-mass stars in Orion, and found X-ray flares in the 0.5–8 keV range with X-ray radiated energies up to 2×10^{35} erg. McCleary & Wolk (2011) studied high-contrast flares in young stars, and found X-ray flares up to about 10^{37} erg.

4.1.1. Determination of Other Parameters for F2

The X-ray decay analysis in Section 3.4 gives a loop semi-length of $l = 2.0 \pm 1.0\ R_\star$. Based on the discussion in Section 3.2, we use constraints on the flare footpoint area from V- and R-band photometry for F2 obtained assuming a color temperature T_{BB} of 6000 K, or $X_{F2,V}(T_{BB} = 6000\,\mathrm{K}) = 0.14$. The total flaring area is $A_{fl} = X_{fl}\pi R_\star^2 = 2\pi R_{foot}^2$. These two numbers constrain the value $\alpha = R_{foot}/(2l)$, assuming a single columnar loop with semi-length l as derived above and two footpoints contributing

Table 5
Comparison of DG CVn BFF and F2 Events with an EV Lac Superflare

	DG CVn BFF	DG CVn F2	EV Lac[a]
Stellar spectral type	M4V	M4V	M3V
Dist. (pc)	18	18	5
Stellar age (MY)	30	30	30–300
Peak temperature T_X[b] (10^6 K)	290	54	139
Peak $\mathcal{VEM}$[c] (10^{54} cm^{-3})	9	1.55	6.3
$\mathcal{VEM}_{\rm expected}$[d] ($10^{54}$ cm^{-3})	2400	1.2	88
$L_{X,\rm peak,0.01-100\ keV}/L_{\rm bol}$	4.8	0.4	3.5
Integrated energy (0.3–10 keV) (10^{34} erg)	40	90	5.8
Integrated energy (V band) (10^{34} erg)	2.8	5.2	…
Footpoint fractional area $X_{\rm fl}$ (10^4 K)	0.375[e]	0.023[e]	>0.03[f]
f_X/f_V	1.9	2.2	4.0
Duration$_X$ (hr)	2.2	6.4	1.7
FWHM$_V$ (s)	20	3600	…
Loop semi-length ($R_\star$)	3.2	2.0 ± 1.0	0.37 ± 0.07
n_e (10^{11} cm^{-3})	3	3	30
$B_{\rm conf}$ (G)	580	230	1100

Notes.
[a] Data for EV Lac taken from Osten et al. (2010).
[b] Peak Temp. from BAT+XRT.
[c] Peak $\mathcal{VEM}$ obtained at different time from peak T.
[d] $\mathcal{VEM}$ expected using $T-\mathcal{VEM}$ scaling of Aschwanden et al. (2008).
[e] Area taken from V band.
[f] Area taken from *Swift* v band.

to the total optical area; the flare area becomes

$$A_{fl} = X_{\rm F2,V}\,\pi R_\star^2 = 2\pi R_{\rm foot}^2, \tag{23}$$

with $R_{\rm foot}$ the radius of one footpoint, and the value $\alpha = R_{\rm foot}/(2l)$ can then be determined to be 0.07 using the vlaue of $X_{\rm F2,V}$ evaluated for $T_{\rm BB} = 6000$ K. This is independent of the number of loops, as long as the loop length l does not change when generalized to N flaring loops. We can couple this with a simple picture of the emitting region as a loop (or N flaring loops), where the volume emission measure can be expressed as

$$\mathcal{VEM} = n_e^2\,\pi R_{\rm foot}^2\,2l. \tag{24}$$

This can be rearranged to give

$$n_e = \left[\frac{\mathcal{VEM}\alpha}{\pi R_\star^3}\left(\frac{X_{\rm F2,V}}{2}\right)^{-3/2}\right]^{1/2} \tag{25}$$

and with the $\mathcal{VEM}$ constrained from the spectrum at peak of F2, and α from the combination of the white-light event and coronal loop length, the coronal electron density is constrained to be 3×10^{11} cm^{-3}. The quantity α in Equation (25) is calculated for $N=1$. Note that this approach can be applied to N flaring loops, and the electron density is unchanged. With n_e and T_X, the strength of the magnetic field required to confine the flaring coronal plasma is then

$$B_{\rm conf} = \sqrt{8\pi n_e k T_X} \tag{26}$$

with k Boltzmann's constant; evaluating this, we derive $B_{\rm conf}$ of ~230 G for F2.

The V-band measurements at the peak of F2 as well as X-ray measurements constrain the flux ratio, which is useful for a comparison of the relative brightening of photospheric and coronal emissions, respectively. At T0+9709 ± 63 s, the Johnson V magnitude is 9.83. This gives a flux density of 4.3×10^{-13} erg cm^{-2} s^{-1} Å^{-1}, or integrated flux over the V filter bandpass of 3.6×10^{-10} erg cm^{-2} s^{-1}, using a FWHM of 836 Å. From Table 2 the 0.3–10 keV flux from the nearest interval, T0+10860:T0+11849 s, is 6.59×10^{-10} erg cm^{-2} s^{-1}. We use the flux estimated in the 0.01–100 keV energy range, 8×10^{-10} erg cm^{-2} s^{-1}, for a flux ratio f_X/f_V of 2.2.

Is $X\sim0.14$ from a 6000 K blackbody reasonable? A preliminary multithread modeling approach to F2 uses the F13 beam heated atmosphere from K13, which were calculated with the RADYN code (Carlsson & Stein 1997). If we assume that the emission during F2 can be modeled by a superposition of impulsively heated loops (new kernels using the "average burst" spectrum (Table 1 of Kowalski et al. 2015; $F_{\rm kernel}$ here)) and decay phase emission from previously heated loops (F13 gradual decay spectrum at $t=4$ s in Table 1 of K15; $F_{\rm decay}$) with an area coverage that is 25 times the kernel emission, then we obtain a broadband spectrum that is generally consistent with the coarse *Swift* UV and optical colors ($uvw2/V\sim1$ compared to the observations ~0.8–0.9). We can estimate an areal coverage using an actual RHD spectrum

$$F_{\rm flare} = 25 * X_{\rm kernel} * F_{\rm decay} + X_{\rm kernel} * F_{\rm kernel} \tag{27}$$

where $F_{\rm kernel}$ is the surface flux of the F13 model averaged over its evolution; $F_{\rm decay}$ is the surface flux of the F13 during the gradual phase.

For the peak of F2, $X_{\rm kernel}=0.008$ and $25*X_{\rm kernel}=0.2$, which is similar to 0.14 for $T=6000$ K. For this modeling, $X(T=10{,}000\ {\rm K})=0.023$ is justified for a nonthermal interpretation and $X(T=6000\ {\rm K})=0.14$ is justified for a thermal (decaying loop) interpretation. In Section 4.1.1, the best area to use is likely the $T=6000$ K area, though the RHD model (at $t=4$ s) that is used to represent the decay emission from previously heated loops is far shorter than the decay times obtained from the X-ray light curves in Section 3. In Figure 8, we show the flare specific luminosity ($L_{\rm flare}=\pi R_{\rm star}^2 F_{\rm flare}$) for the multithread model from RADYN.

Aschwanden et al. (2008), following on earlier work by Shibata & Yokoyama (1999), found a striking similarity between power-law dependences of flare peak volume emission measure against temperature for a sample of solar and stellar flares. The index of the scaling was the same for solar and stellar flares, even while the stellar flare temperatures were generally hotter. The trend, for stars, was $\mathcal{VEM}_p = 10^{50.8}\left(\frac{T_p}{10\ {\rm MK}}\right)^{4.5\pm0.4}$ cm^{-3} with T_p being the flare peak temperature and $\mathcal{VEM}_p$ being the peak volume emission measure of the flare. Using the peak X-ray temperature of F2 from spectroscopic fitting in Section 3.1.2, namely 48 MK, the emission measure expected from this scaling relation is 7×10^{53} cm^{-3}, so only a factor of 2.3 below the observed peak emission measure of 1.64×10^{54} cm^{-3}.

4.2. Interpretation of BFF

Analysis of the BFF event shows that from approximately T0−30 until T0+328 s, the X-ray spectra reveal evidence of

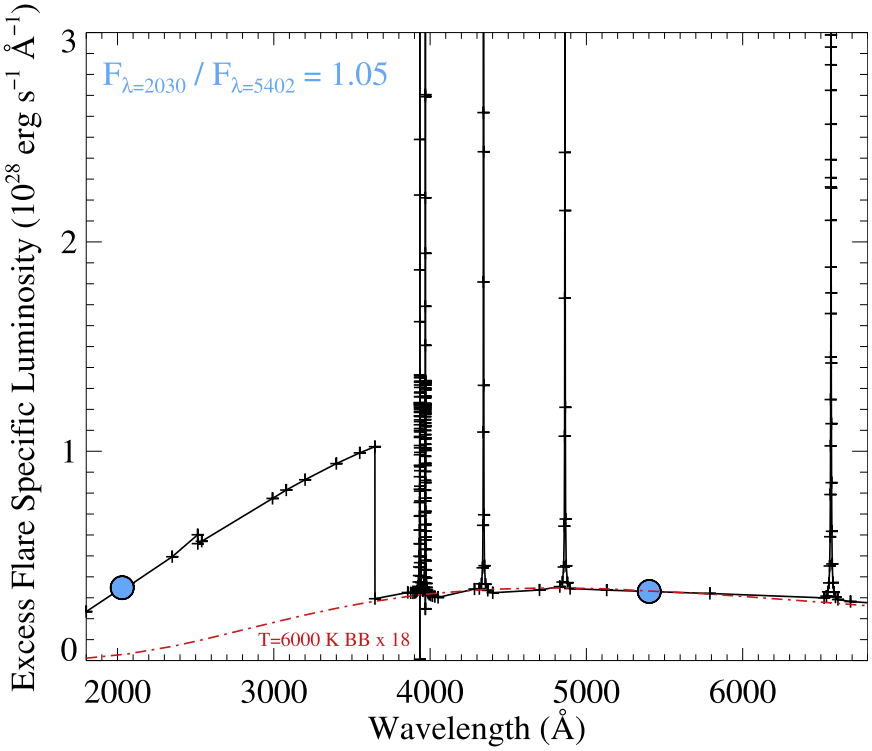

Figure 8. Excess flare specific luminosity calculated using the RADYN code as described in Kowalski et al. (2015); black plusses and solid lines are the RHD calculations. Red dashed–dotted line is the blackbody spectrum at $T_{BB} = 6000$ K. Blue circles are the midpoints of the *uvw2* and *V* filters, respectively, and are used to estimate a flux ratio to be compared against that observed in F2.

either a high-temperature plasma, larger than any seen in previous large stellar flares, or a nonthermal thick-target bremsstrahlung emission. The comparison is especially good in the ∼200 s where both XRT and BAT spectra are available: the XRT+BAT spectrum of BFF is remarkably featureless. Both models are essentially indistinguishable based on the statistics of the model fits to the data, and here we turn to supporting data to aid in our interpretation. We use the supporting data available for BFF, namely the *V*-band measurements, which constrain the flare footpoint area, and the decay of a radio flare starting about 7 minutes after T0 (reported in Fender et al. 2015), from which we have estimated $E_{\rm kin}$ in Section 3.3.5.

X-ray and optical measurements of BFF early after the trigger enables a determination of the ratio of coronal to photospheric emissions. The *V* peak magnitude from Caballero-García et al. (2015) is ∼7, giving a flux of about 5.83×10^{-12} erg cm^{-2} s^{-1} Å^{-1}. Then the estimated *V* filter flux at this time is 4.9×10^{-9} erg cm^{-2} s^{-1}. From Table 1, the 0.3–10 keV flux for BFF at a time near the *V* measurement is 4.5×10^{-9} erg cm^{-2} s^{-1} from T0−30:T0+72, extrapolated from the best-fit model in the 14–100 keV energy range. Because of the large fraction of X-ray flux emitted in the 14–100 keV range, we use the total (0.01–100 keV) energy range estimated to be 9.3×10^{-9} erg cm^{-2} s^{-1}. This leads to a flux ratio f_X/f_V of 1.9, similar to that obtained near the peak of F2.

A lower limit for the estimated 0.3–10 keV X-ray radiated energy of BFF assuming an exponential decay is about 4×10^{35} erg, less than half the radiated energy from F2. The amount of energy radiated in the *V* filter bandpass is about an order of magnitude less than this. Section 3.3.4 discusses the energy partition within BFF and F2; both appear to be X-ray luminous compared to expectations from scaling of optical flare energy to bolometric radiated energy from Osten & Wolk (2015). The integrated *V*-band energy from the EV Lac superflare described in Osten et al. (2010) could not be calculated due to insufficient data, but we note that the large enhancement flare on the very-low-mass star described in Stelzer et al. (2006) had nearly equal amounts of radiated energy in the X-ray and *V* filter bandpasses (but overall lower integrated values, at $\sim 3 \times 10^{32}$ erg).

4.2.1. A Nonthermal Interpretation for BFF

Table 1 lists the best-fit parameters for the trigger spectrum and ≈200 s where both XRT and BAT spectra were obtained, using a nonthermal thick-target bremsstrahlung model for the spectral fitting. The free parameters in the spectral fitting are the index δ_X of the accelerated electrons and the total power in the electron beam.

We have one constraint on the kinetic energy of the accelerated particles involved in the event by multiplying the power from each spectral segment by the integration time for that segment. From the parameters in Table 1, this is a staggering 5×10^{39} erg, and is a lower limit, since there is no X-ray data for a large portion of the event, and the total power depends on the value of the low-energy cutoff, as described in Section 3.1.1. Estimation of the kinetic energy also proceeded from the radio light curve in Section 3.3.5; we use the value of δ_X from the X-ray spectral fits to determine plausible values of kinetic energy. Solar flare data shows that the nonthermal electrons producing nonthermal hard X-ray emission tend to be less energetic than those producing the radio gyrosynchrotron emission, but we assume $\delta_X = \delta_r$ for simplicity. With that substitution, the kinetic energy then becomes a function of the

magnetic field strength in the radio-emitting source, according to Figure 6. Matching the lower limit on kinetic energy implied by a nonthermal interpretation of the X-ray spectrum with the estimated kinetic energy inferred from the analysis of the radio flare requires a very low magnetic field strength, of the order of 20 G or less in the radio-emitting source.

The peak power of the electron beam, derived from spectral fitting, is 3×10^{37} erg s^{-1}. The *V*-band measurement at the peak of BFF gives a constraint on the footpoints of the flaring loop to be $X_{\mathrm{BFF},V} = 0.375$, or an area of 9×10^{20} cm^2. This implies a beam flux of 10^{16} erg cm^{-2} s^{-1}, which is about four orders of magnitude larger than the largest beam fluxes investigated for solar flares ($>5 \times 10^{12}$ erg s^{-1} cm^{-2} Krucker et al. 2011). For an F16 beam, the drift speed of the return current would have to be the speed of light and still the beam would not be neutralized, therefore, resulting in strong magnetic fields. Such a large beam flux seems physically implausible because it would require treatment of a return current and violation of fundamental assumptions, and we do not consider it to be a viable interpretation. Additionally, Caballero-García et al. (2015) argue that the time delay between the optical *V* band burst and the *Swift* trigger is evidence of the Neupert effect, which would be difficult to envisage if the X-ray emission was entirely nonthermal.

4.2.2. A Thermal Interpretation for BFF

The standard flare decay analyses for the X-ray emission done for F2 will not work for BFF, because the temperature is not changing appreciably over the 200 s timescales over which we have X-ray data. Our insight into BFF is guided by an analysis of the F2 event, for which we see $T(t)$, $\mathcal{VEM}(t)$, and from which we can infer coronal loop length, and a ratio of the radius of the loop (from white-light footpoints) to the coronal loop length. For the BFF event, *V*-band data give us the flare footpoint area, and by assuming that the same value of α applies to BFF as well as F2, we can estimate the loop length for BFF. For $\alpha = 0.07$, and the value of $X_{\mathrm{BFF},V} = 0.375$ for a blackbody temperature of 10^4 K, we infer a coronal loop semi-length of 3.2 $R_\star$ or maximum height of 2.0 $R_\star$. Tying these parameters together with the peak $\mathcal{VEM}$ for the thermal model from Table 1 using Equations (25) and (26), we derive n_e of 3×10^{11} cm^{-3}, and a B_{conf} of 580 G. These numbers are similar to what we derive for F2, and given that the energy partition between X-rays and *V* band appears to be similar, the likely case is a thermal plasma.

Table 5 compares key parameters of the two flares considered here on DG CVn, as well as the superflare on the nearby EV Lac described in Osten et al. (2010). The energy comparison is restricted to the energy bands with the most temporal coverage: in EV Lac and BFF there was significant HXR emission in the initial stages of the flare. Note that the estimation of f_V for EV Lac, proceeding using the same steps as described above for the F2 event of DG CVn, yields an integrated *V* filter flux of 6.15×10^{-9} erg cm^{-2} s^{-1}, for a value of f_X/f_V of 4.0. The peak X-ray luminosity relative to bolometric luminosity was calculated over the expanded energy range of 0.01–100 keV to account for the majority of the radiative losses of the hot coronal plasma; the value for EV Lac was taken using parameters in the first line of Table 2 in Osten et al. (2010) and calculated on this larger energy range. Using the scaling relationship between flare temperature and emission measure established for solar flares and a sample of stellar flares, for the DG CVn flare BFF, we would expect a $\mathcal{VEM}$ nearly 2400 times larger than observed, and, for the EV Lac peak flare, a factor of 88 larger than observed (see Table 5). This may be seen as problematic for the thermal interpretation; however, there have been previous suggestions of a departure from this behavior at the highest stellar flare temperatures previously observed. Getman et al. (2008) suggested that superhot flares may turn over in this relationship, based on inferring flare temperatures using a median energy analysis of flares from young stars, and suggested that even at temperatures in excess of 100 MK the $\mathcal{VEM}$ should be between 10^{54} and 10^{55} cm^{-3}.

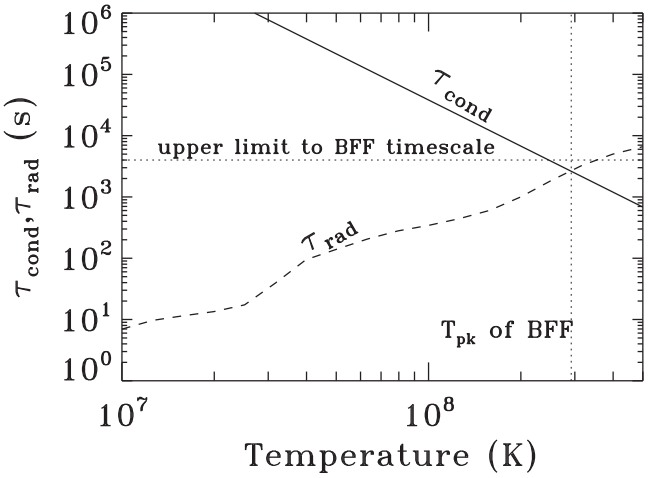

Figure 9. Dependence of conductive and radiative loss times vs. temperature for the BFF event, using electron densities and length scales calculated in the analysis. The location of the peak temperature of BFF derived from X-ray spectral fitting, as well as the upper limit to the timescale of the event, are also shown, and are consistent with the timescale and temperature where the two loss mechanisms are approximately equal.

The high temperatures suggest that the plasma will lose its energy by conductive losses on a relatively fast timescale. The timescale on which the plasma will lose energy by radiative losses

$$\tau_{\mathrm{rad}} = \frac{3 k_{\mathrm{B}} T_e}{n_e \psi(T_e)} \tag{28}$$

depends on the electron density n_e, electron temperature T_e, Boltzmann's constant k_{B}, and the radiative loss function $\psi(T_e)$. The radiative losses for a collisionally ionized plasma are evaluated by summing the contributions from line and continuum radiation at each temperature tabulated in the Astrophysical Plasma Emission Database (Smith et al. 2001), similar to what was done in Osten et al. (2006). The timescale on which the plasma will lose energy by conductive losses is

$$\tau_{\mathrm{cond}} = \frac{3 n_e k_{\mathrm{B}} l^2}{\kappa T_e^{5/2}} \tag{29}$$

where l is the length scale and κ is the Spitzer conductivity coefficient ($=8.8 \times 10^{-7}$ erg cm^{-1} s^{-1} K$^{-7/2}$ Spitzer 1962). Using values for electron density and length scale derived from analyses above, we determine the dependence of the two timescales on electron temperature and compare with the duration and peak temperature of BFF. Figure 9 displays the results. It is curious that the location at which the two timescales are approximately equal is close to the peak

temperature of BFF, and the value of the timescales are similar to the upper limit given to the event duration of BFF from the sparse data.

Given the extreme parameters of BFF, we can also examine the ratio of the relaxation time of the plasma to the conductive cooling time. In order for such a hot temperature plasma to be observed, the relaxation time should not be larger than the timescale on which the plasma lose energy by conduction. The ratio of the thermal relaxation time of the plasma to the timescale for conductive cooling is

$$\tau_{\rm relax}/\tau_{\rm cond} = 2\frac{T_8^4}{n_{11}^2 L_9^2} \quad (30)$$

(see the discussion in Benz 2002), where T_8 is the temperature in units of 10^8 K, n_{11} is the electron density in units of 10^{11} cm^{-3}, and L_9 is the loop length in units of 10^9 cm. Evaluating Equation (30) for the values appropriate for this flare, we find $\tau_{\rm relax}/\tau_{\rm cond}$ to be 2×10^{-4}. This demonstrates that the plasma does have time to relax to the observed thermal temperature.

The total kinetic energy in BFF cannot be constrained independently for a thermal interpretation of BFF; the results from Section 3.3.4 show it to depend on δ and B. However, an estimate for a lower limit to the total radiated X-ray energy for BFF is 4×10^{35} erg. Studies of the global energetics of large solar flares (Emslie et al. 2012) show that the total radiation from soft X-ray emitting plasma is comparable to or slightly smaller than the energy in flare electrons accelerated to energies greater than 20 keV. If we assume that the energy partition is similar for BFF, then a rough equipartition between the radiated X-ray energy and the energy in accelerated electrons would suggest, via Figure 6, magnetic field strengths in the radio-emitting plasma of several hundred Gauss to about 1 kiloGauss. This is consistent with the field strengths derived above independently from equipartition between the gas pressure and magnetic pressure.

If we take the thermal interpretation as the more physically plausible explanation, given the constraints from the multi-wavelength observations, then we can still ask the question of what signature of nonthermal electrons might be expected to appear in the hard X-ray spectral range. Nonthermal particles propagate in a collisionless plasma. A lower limit to the particle energy required to cross a propagation path with length L across a density n_e is given by setting the propagation time of accelerated electrons equal to the collisional deflection time (Aschwanden 2002)

$$E \geqslant 20\sqrt{L_9 n_{11}\left(\frac{0.7}{\cos\alpha}\right)} \quad \text{keV} \quad (31)$$

where L_9 is the loop length in units of 10^9 cm, n_{11} is the electron density in units of 10^{11} cm^{-3}, and α is the pitch angle. For the parameters in Table 5 the minimum energy is 580 keV; this analysis suggests that the accelerated particles filling the entire flare loop would produce nonthermal hard X-ray emission at energies above this to be potentially observable.

4.3. Implications

The two large flares studied on DG CVn in this paper are both an order of magnitude larger than the individual flares on nearby M dwarfs previously studied in detail, and they also eclipse the radiated energies of the largest flares seen on much younger stars not amenable to detailed study. It is remarkable that in one data set we have possibly the top two most energetic X-ray flares from a low-mass star that have been detected to date. The large stellar flares on M dwarfs previously studied in detail have tended to be much lower in energy and amplitude. This is understandable as the frequency of occurrence of large flares declines with both increasing energy and peak luminosity. Caramazza et al. (2007) reported on X-ray flares occurring on ~1 MY old solar-mass and low-mass stars, with the low-mass stars having flares with radiated energies in the 0.3–8 keV bandpass of up to $\sim 2 \times 10^{35}$ erg. Due to the larger distances of the low-mass flaring stars in their sample (at the distance of the Orion Nebula Cluster, or ≈450 pc), detailed study of the X-ray flares was not possible, and there was no accompanying multi-wavelength information.

We do not have solid constraints on the frequency of events of this large size. Tsuboi et al. (2014) reported approximately four stellar flares from active M dwarfs with energies in the range of 10^{35}–10^{36}, which are not upper limits, from four years' worth of monitoring of the hard X-ray sky with the MAXI/GSC instrument, which suggests an upper bound occurrence rate of roughly one flare per year per star. If we use flare frequency distributions for an active M dwarf and extrapolate to these energies, then we can get a lower bound on the occurrence rate. Lacy et al. (1976) calculated flare frequencies for a sample of nearby active M dwarfs using integrated U-band energies. From Table 4, we have estimated the U-band energies for BFF and F2, respectively. Using the three single flare stars in Lacy et al. (1976), which had the largest flare energies in that paper, namely YZ CMi, EQ Peg, and EV Lac, we calculate the expected occurrence rate for flares exceeding 4.7×10^{34} erg (E_U for BFF) to be once every (68, 388, 69) days for (YZ CMi, EQ Peg, and EV Lac), respectively. If we consider the two events combined to be a single large eruptive event, then the occurrence rate of such energetic events, which together total $E_U = 1.3 \times 10^{35}$ erg, is once every (141, 1080, 140) days for the flare frequency distribution parameters from YZ CMi, EQ Peg, and EV Lac. These estimates vary by a factor of 10 from each other, and reflect not only the uncertainty in flare to flare differences in flare frequency distributions, but also uncertainty in the behavior of the flare frequency distribution itself; namely whether the occurrence rate of flares at such high energies continues to follow a power-law distribution. These estimates are also about a factor of three from the estimate using Tsuboi et al. (2014) indicating general agreement at about that level.

These events are also far larger than the event studied in detail to determine the likely astrobiological effects of stellar flares on close-in terrestrial exoplanets, and have coverage in both the UV/optical and X-ray bandpasses. Given the estimated occurrence rate, they will be an important contributor in shaping the radiation and particle environment around an M dwarf in which extrasolar planets will be forming and existing. Segura et al. (2010) utilized UV-optical observations of the Great Flare on AD Leo, which had an integrated energy in the 1200–8000 Å range of $\sim 10^{34}$ erg. They used scalings between UV radiated energy and X-ray energy, and a further scaling of X-ray flux to proton flux, to model the response of a terrestrial atmosphere to the impingement of the UV flare photons only or the flare photons along with the MeV energy protons. We note that the comparison of the R-band-radiated energy of F2 on DG CVn to the Great Flare on AD Leo in our Figure 4 reveals

F2 to be a factor of ≈20 larger. The energetic protons, which were modelled, removed the ozone layer, on timescales of about two years, and the recovery time of the planetary atmosphere was a few decades. These effects coupled with the esimated occurrence rate of even larger events suggests that there might be a permanent erosion of the ozone layer. One critical open question in this area is whether the scalings observed in solar eruptive events between photons and particles holds during stellar events. A more recent paper on the effects of stellar flares on exoplanetary atmospheres (Venot et al. 2016) determined that planets around very active stars would likely never achieve a steady state due to the frequent photon bombardment of the exoplanetary atmosphere from stellar flares.

Smith et al. (2004) considered the transport of ionizing radiation in terrestrial exoplanet atmospheres, and found that while a thick atmosphere can protect the planetary surface from incident X-rays and γ-rays, up to 4% of the incident ionizing radiation received at the surface in the 2000–3200 Å wavelength range comes from atmospheric transmission and reprocessing of the high-energy radiation. Because the two flares reported here have peak X-ray luminosities more than several hundred times larger than the quiescent values, any irradiation of a planetary atmosphere would increase temporarily by the same large factor. The effect of such large variations in the stellar ionizing flux may be significant, especially early in the life of the star and planetary system. The previous studies examining the impact of stellar flares on exoplanet atmospheres, like Segura et al. (2010) and Venot et al. (2016), used only UV observations, ignoring the potential increase in UV emission incident on the planet due to high-energy photons in the manner described in Smith et al. (2004). Hence they are underestimates at best of the impact of these flares on exoplanet atmospheric chemistry.

The flaring star that produced these immense energetic releases is not solitary, which raises the question of whether the companion could have any impact on the existence of these superflares. The DG CVn system is a binary, with the two stars separated by ∼4 au. At their young age the components are not yet tidally synchronized, precluding an origin in increased magnetic activity from tidal interaction akin to that seen in RS CVn or BY Dra systems. Recent studies of M dwarf-white dwarf binary systems suggest that even non-interacting close binaries (<10 au separation) may have a higher flare rate than single stars (Morgan et al. 2016), though Stern et al. (1995) found no correlation between X-ray luminosity and orbital period for spectroscopic binaries in the Hyades with periods greater than 10 days. Whether this can be related to dynamical interaction within a circumbinary disk compared to the evolution of a circumstellar disk is speculative. However, since single M dwarf flare stars are also capable of producing stellar superflares with roughly similar characteristics (Table 5) this suggests that the binarity is not a strong factor.

5. CONCLUSIONS

We presented a detailed study of two of the most energetic flare events seen on a young low-mass star. In addition to measurements made for each flare event, we used the properties of the second flare F2 to infer some of the properties for BFF. The results confirmed the basic flare scenario for hyperactive stars as for solar flares, and revealed evidence of departures of trends between the temperatures and emission measures of the highest temperature stellar flares compared with lower temperature solar flares. The object, DG CVn, has been relatively uncharacterized for its flaring and extreme magnetic activity and we hope that this report will spur additional studies. Based on the flare properties described in this paper, we expect the existence of very strong magnetic fields in the photosphere. Starspot modeling should confirm the nature of starspot sizes implied by the flare footpoint modeling. Uncertainties in the rotation period and $v \sin i$ mentioned in the introduction are likely the result of the previously unrecognized binary nature of the system.

While X-ray flares from stars are commonly known, observations with *Swift* have revealed that stellar flares can be bright enough to trigger the BAT with their intense hard X-ray (>15 keV) emission. These events reveal the nature of magnetic reconnection processes occurring in a regime vastly different from the Sun, yet exhibiting continuity with solar events. Supporting data from both space- and ground-based observatories enable more constraints on the extremes of energetics and plasma parameters. In contrast with the claim of nonthermal emission from the superflare on II Peg reported by Osten et al. (2007), for the DG CVn event the possibility of a nonthermal interpretation is confronted with constraints on kinetic energy and photospheric flare area provided by radio and optical observations, respectively. Since the nonthermal interpretation is disfavored in the DG CVn flares because of constraints from the radio and optical data, the II Peg nonthermal interpretation is in doubt.

The extreme nature of the flare temperature of BFF, coupled with results from other extreme flares, suggest that the scaling between solar and stellar flare temperatures and emission measures exhibits a flattening at high temperatures. The opportunity these flares present to confirm this flattening by using spectroscopically derived temperatures is important and may reveal departures from canonical solar flare behavior.

Planets around M dwarfs will likely experience millions of these kinds of superflares during their infancy. This pair of well-studied flares on M dwarfs should be used to provide updated constraints on the impact of flare radiation on close-in terrestrial exoplanets. This confirms the conclusion reached for EV Lac that the "habitable zone" ∼0.1 au from a young M dwarf star is likely inimicable to life: the flare peak luminosity in the *GOES* (1.5–8 keV) band would be equivalent to an X60,000,000 flare. If the energetic proton fluxes and coronal mass ejection energies scale with the radiated flare energy, the impact upon the atmosphere and magnetosphere of any hypothetical terrestrial planet would be catastrophic.

This work made use of data supplied by the UK *Swift* Science Data Centre at the University of Leicester. This publication makes use of data products from the *Wide-field Infrared Survey Explorer*, which is a joint project of the University of California, Los Angeles, and the Jet Propulsion Laboratory/California Institute of Technology, funded by the National Aeronautics and Space Administration. S.R.O. also acknowledges the support of the Spanish Ministry, Project Number AYA2012-39727-C03-01. This publication makes use of data products from the Wide-field Infrared Survey Explorer, which is a joint project of the University of California, Los Angeles, and the Jet Propulsion Laboratory/California Institute of Technology, funded by the National Aeronautics and Space Administration. We acknowledge the support from the *Swift*

project (N. Gehrels) and *Swift* schedulers at Penn State, which enabled the acquisition of this wonderful data set. R.A.O. and A.K. acknowledge fruitful discussions at ISSI in Bern with the Energy Transformation in Solar and Stellar Flares team during the preparation of this manuscript.

REFERENCES

Aschwanden, M. J. 2002, SSRv, 101, 1
Aschwanden, M. J., Stern, R. A., & Güdel, M. 2008, ApJ, 672, 659
Barthelmy, S. D., Barbier, L. M., Cummings, J. R., et al. 2005, SSRv, 120, 143
Beers, T. C., Bestman, W., & Wilhelm, R. 1994, AJ, 108, 268
Benz, A. 2002, Plasma Astrophysics: Kinetic Processes in Solar and Stellar Coronae, Vol. 279 (2nd ed.; Dordrecht: Kluwer)
Benz, A. O., & Güdel, M. 2010, ARA&A, 48, 241
Beuzit, J.-L., Ségransan, D., Forveille, T., et al. 2004, A&A, 425, 997
Breeveld, A. A., Landsman, W., Holland, S. T., et al. 2011, in AIP Conf. Ser. 1358, Gamma Ray Bursts 2010, ed. J. E. McEnery, J. L. Racusin, & N. Gehrels (Melville, NY: AIP), 373
Brickhouse, N. S., Cranmer, S. R., Dupree, A. K., Luna, G. J. M., & Wolk, S. 2010, ApJ, 710, 1835
Burrows, D. N., Hill, J. E., Nousek, J. A., et al. 2005, SSRv, 120, 165
Caballero-García, M. D., Šimon, V., Jelínek, M., et al. 2015, MNRAS, 452, 4195
Caramazza, M., Flaccomio, E., Micela, G., et al. 2007, A&A, 471, 645
Carlsson, M., & Stein, R. F. 1997, ApJ, 481, 500
Chrastina, M., & Hroch, F. 2008, OEJV, 95, 21
Cutri, R. M., Wright, E. L., Conrow, T., et al. 2013, Explanatory Supplement to the AllWISE Data Release Products, 2328
Demory, B.-O., Ségransan, D., Forveille, T., et al. 2009, A&A, 505, 205
Dennis, B. R., & Schwartz, R. A. 1989, SoPh, 121, 75
Drake, S., Osten, R., Page, K. L., et al. 2014, ATel, 6121, 1
Dulk, G. A. 1985, ARA&A, 23, 169
Emslie, A. G., Dennis, B. R., Shih, A. Y., et al. 2012, ApJ, 759, 71
Evans, P. A., Beardmore, A. P., Page, K. L., et al. 2007, A&A, 469, 379
Evans, P. A., Beardmore, A. P., Page, K. L., et al. 2009, MNRAS, 397, 1177
Favata, F., Flaccomio, E., Reale, F., et al. 2005, ApJS, 160, 469
Fender, R. P., Anderson, G. E., Osten, R., et al. 2015, MNRAS, 446, L66
Gershberg, R. E. 1972, Ap&SS, 19, 75
Getman, K. V., Feigelson, E. D., Broos, P. S., Micela, G., & Garmire, G. P. 2008, ApJ, 688, 418
Gizis, J. E., Reid, I. N., & Hawley, S. L. 2002, AJ, 123, 3356
Hawley, S. L., Allred, J. C., Johns-Krull, C. M., et al. 2003, ApJ, 597, 535
Hawley, S. L., & Fisher, G. H. 1992, ApJS, 78, 565
Hawley, S. L., & Pettersen, B. R. 1991, ApJ, 378, 725
Helfand, D. J., Schnee, S., Becker, R. H., White, R. L., & McMahon, R. G. 1999, AJ, 117, 1568
Hünsch, M., Schmitt, J. H. M. M., Sterzik, M. F., & Voges, W. 1999, A&AS, 135, 319
Kontar, E. P., Dickson, E., & Kašparová, J. 2008, SoPh, 252, 139
Kowalski, A. F., Hawley, S. L., Carlsson, M., et al. 2015, SoPh, 290, 3487
Kowalski, A. F., Hawley, S. L., Holtzman, J. A., Wisniewski, J. P., & Hilton, E. J. 2010, ApJL, 714, L98
Kowalski, A. F., Hawley, S. L., Holtzman, J. A., Wisniewski, J. P., & Hilton, E. J. 2012, SoPh, 277, 21
Kowalski, A. F., Hawley, S. L., Wisniewski, J. P., et al. 2013, ApJS, 207, 15
Krucker, S., Hudson, H. S., Jeffrey, N. L. S., et al. 2011, ApJ, 739, 96
Kuerster, M., & Schmitt, J. H. M. M. 1996, A&A, 311, 211
Lacy, C. H., Moffett, T. J., & Evans, D. S. 1976, ApJS, 30, 85
Lee, J., & Gary, D. E. 2000, ApJ, 543, 457
Lin, R. P. 2011, SSRv, 159, 421
Malamut, C., Redfield, S., Linsky, J. L., Wood, B. E., & Ayres, T. R. 2014, ApJ, 787, 75
Mann, A. W., Feiden, G. A., Gaidos, E., Boyajian, T., & von Braun, K. 2015, ApJ, 804, 64
McCleary, J. E., & Wolk, S. J. 2011, AJ, 141, 201
Meibom, S., Mathieu, R. D., & Stassun, K. G. 2007, ApJL, 665, L155
Mohanty, S., & Basri, G. 2003, ApJ, 583, 451
Morgan, D. P., West, A. A., & Becker, A. C. 2016, AJ, 151, 114
Newton, E. R., Charbonneau, D., Irwin, J., & Mann, A. W. 2015, ApJ, 800, 85
Osten, R. A., Drake, S., Tueller, J., et al. 2007, ApJ, 654, 1052
Osten, R. A., Godet, O., Drake, S., et al. 2010, ApJ, 721, 785
Osten, R. A., Hawley, S. L., Allred, J., et al. 2006, ApJ, 647, 1349
Osten, R. A., Hawley, S. L., Allred, J. C., Johns-Krull, C. M., & Roark, C. 2005, ApJ, 621, 398
Osten, R. A., & Wolk, S. J. 2015, ApJ, 809, 79
Pagani, C., Beardmore, A. P., Abbey, A. F., et al. 2011, A&A, 534, A20
Page, M. J., Kuin, N. P. M., Breeveld, A. A., et al. 2013, MNRAS, 436, 1684
Parker, E. N. 1988, ApJ, 330, 474
Reale, F., Micela, G., Peres, G., Betta, R., & Serio, S. 1997, MmSAI, 68, 1103
Riedel, A. R., Finch, C. T., Henry, T. J., et al. 2014, AJ, 147, 85
Robb, R. 1994, in ASP Conf. Ser. 55, Optical Astronomy from the Earth and Moon, ed. D. M. Pyper & R. J. Angione (San Francisco, CA: ASP), 246
Roming, P. W. A., Kennedy, T. E., Mason, K. O., et al. 2005, SSRv, 120, 95
Schmidt, S. J., Prieto, J. L., Stanek, K. Z., et al. 2014, ApJL, 781, L24
Segura, A., Walkowicz, L. M., Meadows, V., Kasting, J., & Hawley, S. 2010, AsBio, 10, 751
Serio, S., Reale, F., Jakimiec, J., Sylwester, B., & Sylwester, J. 1991, A&A, 241, 197
Sharykin, I. N., Struminskii, A. B., & Zimovets, I. V. 2015, AstL, 41, 53
Shibata, K., & Yokoyama, T. 1999, ApJL, 526, L49
Smith, D. S., Scalo, J., & Wheeler, J. C. 2004, Icar, 171, 229
Smith, K., Güdel, M., & Audard, M. 2005, A&A, 436, 241
Smith, R. K., Brickhouse, N. S., Liedahl, D. A., & Raymond, J. C. 2001, ApJL, 556, L91
Spitzer, L. 1962, Physics of Fully Ionized Gases (2nd ed.; New York: Interscience)
Stassun, K. G., van den Berg, M., Feigelson, E., & Flaccomio, E. 2006, ApJ, 649, 914
Stelzer, B., Schmitt, J. H. M. M., Micela, G., & Liefke, C. 2006, A&A, 460, L35
Stern, R. A., Schmitt, J. H. M. M., & Kahabka, P. T. 1995, ApJ, 448, 683
Tsuboi, Y., Higa, M., Yamazaki, K. & MAXI Team 2014, Suzaku-MAXI 2014: Expanding the Frontiers of the X-ray Universe, ed. M. Ishida, R. Petre, & K. Mitsuda, 138, www.xray.ess.sci.osaka-u.ac.jp/SuzakuMAXI2014/proceedings.html
Venot, O., Rocchetto, M., Carl, S., Hashim, A., & Decin, L. 2016, arXiv:1607.08147